Remote Sensing of Environment 305 (2024) 114061

Contents lists available at ScienceDirect

Remote Sensing of Environment

journal homepage: www.elsevier.com/locate/rse

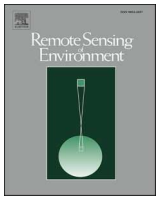

Solar-induced chlorophyll fluorescence sheds light on global evapotranspiration

Quan Zhang [a,*], Xuanqi Liu [a], Kai Zhou [b], Yang Zhou [a], Pierre Gentine [c,d], Ming Pan [e], Gabriel G. Katul [f]

[a] State Key Laboratory of Water Resources Engineering and Management, Wuhan University, Wuhan, China
[b] Bureau of Hydrology, Changjiang Water Resources Commission, Wuhan, China
[c] Department of Earth and Environmental Engineering, Columbia University, New York, NY, USA
[d] Center for Learning the Earth with Artificial intelligence and Physics (LEAP), Columbia University, New York, NY, USA
[e] Center for Western Weather and Water Extremes, Scripps Institution of Oceanography, University of California San Diego, La Jolla, CA, USA
[f] Department of Civil and Environmental Engineering, Duke University, Durham, NC, USA

ARTICLE INFO

Editor: Jing M. Chen

Keywords:
Evapotranspiration
Optimal stomatal conductance theory
Solar-induced fluorescence
Water-carbon relations
Global hydrological cycle

ABSTRACT

The significance of large-scale evapotranspiration (ET) to climate science, water resources management, flood routing, irreversible desertification, and crop yield is not in dispute. Current large-scale ET models combine empirical formulations with a suite of remotely sensed data products that include meteorological variables, vegetation indices and/or soil moisture. In recent years, solar-induced chlorophyll fluorescence (SIF) has been proposed as an indicator of photosynthetic activity but its potential to constrain transpiration (T_r) or ET remains under-explored and frames the scope here. A large-scale terrestrial ET model driven by SIF is developed based on leaf water-carbon exchange complemented with an outcome for intercellular to ambient CO_2 concentration derived from optimality theory for stomatal conductance. The model parameters are first calibrated across FLUXNET sites and then extrapolated globally using their dependence on climatic variables and plant functional types. The model, hereafter referred to as ET_{SIF}, requires SIF data, leaf area index, land use type, and basic meteorological variables that include net radiation, air temperature and relative humidity. Global ET_{SIF} estimates computed on a 4-day window for the period spanning 2003 to 2018 was 625 mm yr^{-1} in general agreement with other independent global ET estimates, but discrepancy in the spatial distribution still exists implying that global ET estimation remains subject to large uncertainty. ET_{SIF} exhibited a tantalizing positive trend over the same period but this trend was not statistically significant. One of the major advantages of this new approach, is that the model requires few parameters, reduce the parameterization of stomatal conductance and can be immediately used to constrain spatially extended ET estimates.

1. Introduction

Evapotranspiration (ET) is the main terrestrial pathway by which precipitation is recycled back to the atmosphere. The significance of this water flux in regulating the climate system has been recognized since the late 1970s (Eagleson, 1981) and much recent attention is focused on its interaction with the terrestrial carbon cycle (Jung et al., 2010). Because of the large latent heat of vaporization value of water, the ET cooling effects also regulate land-surface and near-surface air temperatures (Oki and Kanae, 2006; Gentine et al., 2010, 2011; Zhang et al., 2020). Estimates of global ET are required for assessing shifts in the hydrological cycle, drought monitoring (McEvoy et al., 2016), and climate change model evaluation. Unsurprisingly, estimating ET at spatially extended scales using remote sensing products continues to receive research interest (e.g., Bastiaanssen et al., 1998; Su, 2002; Mu et al., 2007, 2011; Yuan et al., 2010; Martens et al., 2017). Barriers to estimating ET at such large spatial scales include difficulties in capturing heterogeneity in soil-vegetation activity and the complex interactive effects of biochemical and biophysical processes regulating transpiration (T_r).

Prior remote sensing-based approaches to estimating ET at global scales fall into two broad categories: (i) meteorologically based semi-empirical methods and (ii) surface energy balance residual methods.

* Corresponding author.
E-mail addresses: quan.zhang@whu.edu.cn (Q. Zhang), 2022282060179@whu.edu.cn (X. Liu), 2020302191810@whu.edu.cn (Y. Zhou), pg2328@columbia.edu (P. Gentine), m3pan@ucsd.edu (M. Pan), gaby@duke.edu (G.G. Katul).

https://doi.org/10.1016/j.rse.2024.114061
Received 29 June 2023; Received in revised form 21 January 2024; Accepted 16 February 2024
Available online 1 March 2024

The meteorologically based methods employ a Penman equation (Penman, 1948) or variants such as the Penman-Monteith (PM) equation (Monteith, 1965) or a Priestley-Taylor (PT) equation (Priestley and Taylor, 1972) to estimate global ET using remotely-sensed vegetation properties, meteorological conditions, near-surface soil water content, among other variables. Mu et al. (2007, 2011) produced a widely used global ET dataset (i.e., MOD16) employing the PM equation, yet in this approach, the stomatal conductance must be parameterized leading to uncertainties in the retrieval. Fisher et al. (2008) modified the PT eq. (PT-JPL) and partitioned ET into three components: evaporation from the soil or forest floor, evaporation of canopy intercepted water, and transpiration T_r. These methods are subject to uncertainties given the difficulty in representing these processes, especially T_r. Another limitation encountered by these models is their ability to reproduce the hysteresis response of ET to radiation load or vapor pressure deficit variation (Zhang et al., 2014c; Lin et al., 2019; Wan et al., 2023). To overcome some of these issues, Yang et al. (2013) used the water - carbon gas exchange relation at the leaf level to link leaf transpiration to photosynthesis, though uncertainties in describing carbon fluxes and their bridge to water fluxes remain. The energy balance residual methods also gained attention because of their simplicity as in the SEBS model (Su, 2002), SEBAL (Bastiaanssen et al., 1998), and other multiple water sources models (e.g., two sources - TSEB, Norman et al., 1995; three sources - 3SEB, Burchard-Levine et al., 2022). Such energy balance residual methods are sensitive to estimates of land-surface temperature and air temperature given that their differential value drives sensible heat fluxes (Zhang et al., 2016b). Moreover, accurate parameterizations do require turbulent flow statistics rarely available at large scales (Katul et al., 1998).

Solar-Induced chlorophyll Fluorescence (SIF) provides a novel way of monitoring large-scale photosynthetic vegetation activity (Sun et al., 2023). Since stomata regulate leaf gas exchange of carbon dioxide and water vapor with the atmosphere, SIF offers a promising way to indirectly infer T_r, framing the scope here. Plants utilize absorbed photosynthetically active radiation (APAR) for photosynthetic activities and dissipate the excessive radiation through non-photochemical quenching (NPQ) processes, and the remaining unexploited APAR in the 400–700 nm spectral range is re-emitted by chlorophyll molecules at longer wavelengths, which is known as solar-induced chlorophyll fluorescence (or SIF). As such, SIF contains key information on plants' photosynthetic activities (Sun et al., 2023) that shows great potentials to constrain T_r. SIF has already been widely used to reconstruct large-scale photosynthesis (Zarco-Tejada et al., 2009; Sun et al., 2015; Yoshida et al., 2015; Zhang et al., 2016a) after Guanter Palomar (2006) performed the first space-based SIF retrieval. From then on, several satellite projects have been launched with equipment allowing for SIF retrievals on board such as the Greenhouse gases Observing SATellite (GOSAT) (Hamazaki et al., 2005; Guanter et al., 2012) and GOSAT2 (Imasu et al., 2023) missions, Global Ozone Monitoring Experiment-2 (GOME-2) (Joiner et al., 2013), Orbiting Carbon Observatory-2 (OCO-2) (Frankenberg et al., 2014) and OCO-3 (Taylor et al., 2020), and TROPOMI (the TROPOspheric Monitoring Instrument) (Köhler et al., 2018), among others. Because SIF can reflect plants' activity, the observed remotely sensed SIF has the potential to constrain large-scale T_r, and thus ET as transpiration is usually the largest fraction of ET, without extensive data needs for meteorological variables and vegetation conditions and their empirical calibrations. The accuracy of the corresponding T_r and ET logically depends on the quality of remote sensing SIF retrievals.

A handful of prior studies already used SIF to model ET empirically. Alemohammad et al. (2017) showed that SIF observations could be used to constrain variations in ET; Damm et al. (2018) found a non-linear relation between ET and SIF while other studies also found that the radiation and meteorological conditions such as Photosynthetically Active Radiation (PAR), Vapor Pressure Deficit (VPD), and Air Temperature (T_a) impact the empirical relation between ET and SIF (e.g., Lu et al., 2018); other studies applied the Penman-Monteith equation by parameterizing canopy conductance (or resistance) using SIF and reported good performance in ET modelling (e.g., Shan et al., 2019; Damm et al., 2021). Utilizing the photosynthetic information contained in SIF products at FLUXNET sites, a method based on water-carbon relations was earlier proposed to estimate ET and tested across these sites (Zhou et al., 2022). In particular, the transpiration-SIF relation was improved when scaled by VPD. The key advantage of the aforementioned model is that it does not require explicit accounting for stomatal conductance. The model reliably reproduced site-level ET when complemented with a soil evaporation model across all land use types. Expanding on this work, the aim here is to (1) determine the ET-SIF model parameters at FLUXNET sites; (2) derive global distributions of the model parameters using their dependences on climatic properties and land use types as derived from FLUXNET analysis; (3) use the outcomes in (1) and (2) to produce a first global terrestrial ET dataset using SIF. Comparison with other global ET products are also discussed at annual and seasonal time scales. It is to be underscored that sublimation over snow and ice and open-water evaporation were not incorporated.

2. Data and method

2.1. Model description of ET using remotely sensed SIF

The ET model proposed here considers three components: Transpiration, T_r, soil evaporation E_s and canopy intercepted water evaporation E_i ($ET = T_r + E_s + E_i$). For simplicity, the ecosystem is assumed to be well coupled with the atmosphere and the water flux from leaves, soil surface and wet canopy are treated as total evapotranspiration. The three components T_r, E_s and E_i are modeled separately but only T_r, the dominant term in ET, is linked with remotely sensed SIF. The T_r model is based on water-carbon relations and commences by linking gross primary productivity (GPP) to SIF linearly (Zhang et al., 2014a; Zhang et al., 2016b; Guanter et al., 2014) as,

$$\mathrm{GPP} = \alpha \mathrm{SIF} + \beta \tag{1}$$

where α is a vegetation specific parameter that relates GPP (μmol m^{-2} s^{-1}) to SIF (mW m^{-2} nm^{-1} sr^{-1}), β (μmol m^{-2} s^{-1}) is an intercept to be determined. Though some studies adopted a nonlinear relation between GPP and SIF (e.g., Guanter et al., 2014; Wei et al., 2018; Gu et al., 2019), we found no discernible difference in the model accuracy for ET when using a more complicated model structure (e.g., Guan et al., 2016; Gu et al., 2019) when compared to a linear one as shown in prior studies (Zhou et al., 2022). Therefore, the linear form in Eq. (1) is adopted throughout to describe the relation between GPP and SIF at all FLUXNET sites. A plausibility argument for Eq. (1) is that the GPP - SIF relation should be close to linear at large spatial scales and over extended (e.g., 4 day in this study) time intervals due to inherent space-time averaging that 'smooths-out' nonlinearities (Zhang et al., 2014a; Gu et al., 2019).

To describe plant photosynthesis at the canopy scale (presumed to approximate GPP), carbon dioxide supply from the atmosphere to the canopy is assumed to be described by a Fickian diffusion that is path-averaged and given as (Katul et al., 2000),

$$\mathrm{GPP} = g_c \bullet C_a \left(1 - \frac{C_i}{C_a}\right) \tag{2}$$

where g_c (mol m^{-2} s^{-1}) is the canopy stomatal conductance to CO_2, C_a is the ambient atmospheric CO_2 concentration (ppm), and C_i is the intercellular CO_2 concentration (ppm). Measured C_a above the canopy was used in all FLUXNET site calibration stages, while the global averaged C_a over time was adopted in the global ET modelling stage (described later). Similarly, T_r can be described using Dalton's law as,

$$T_r = g_w \bullet D \tag{3}$$

where g_w (mol m^{-2} s^{-1}) is the stomatal conductance to water vapor

(g_w=1.6g_c) when CO_2 and water vapor share the same pathway (Katul et al., 2000), D is the water vapor deficit fraction expressed by the molar ratio determined from VPD/P_a, P_a is the atmospheric pressure set as a constant 100 kPa for simplicity, and VPD is, as before, the vapor pressure deficit (kPa). Combing Eqs. (1), (2), and (3) to eliminate stomatal conductance results in,

$$\frac{T_r}{\alpha \mathrm{SIF}+\beta}=\frac{VPD}{P_a C_a}\frac{1.6}{\left(1-\frac{C_i}{C_a}\right)} \tag{4}$$

Re-arranging Eq. (4) to obtain T_r yields,

$$T_r=\frac{1.6VPD(\alpha \mathrm{SIF}+\beta)}{C_a\left(1-\frac{C_i}{C_a}\right)P_a} \tag{5}$$

A major advantage of this approach is that it eliminates the need for modelling g_c and its associated uncertainty; however, C_i/C_a must be externally supplied instead or estimated using models. The simplest model assumes C_i/C_a is a constant determined empirically for each plant functional type. Alternatively, stomatal optimization theories can be adopted instead without adding new parameters. In these theories, stomata are assumed to operate to maximize carbon gain but are constrained by water loss from the soil (Farquhar et al., 1993). In their most simplified form, and upon assuming a linear biochemical demand function, these stomatal optimization theories predict C_i/C_a as (Farquhar et al., 1993; Katul et al., 2009, 2010; Way et al., 2014),

$$\frac{C_i}{C_a}=1-\sqrt{\frac{1.6D\left(C_a-\frac{\Gamma}{\eta}\right)}{\lambda_{cf}C_a^2}} \tag{6}$$

where λ_{cf}(mol mol^{-1}) is the inverse of the marginal water use efficiency presumed to depend on PFTs, Γ (ppm) is the leaf CO_2 compensation point in the absence of mitochondrial respiration, and η is a parameter that distinguishes C3 from C4 plants and is related to the strength of the CO_2 pump in C4 plants. The parameter η is set to unity for C3 plants (no CO_2 pump) but $\eta > 1$ for C4 plants as discussed elsewhere (Way et al., 2014). Hereafter, it is assumed throughout that C3 plants are the dominant species ($\eta = 1$) for simplicity and for pragmatic reasons. With these simplifications, and upon replacing C_i/C_a in Eq. (5) into Eq. (6) yields,

$$T_r=\frac{(\alpha \mathrm{SIF}+\beta)\sqrt{1.6\lambda_{cf}}}{\sqrt{P_a(C_a-\Gamma)}}\mathrm{VPD}^{1/2} \tag{7}$$

A number of features are now pointed out about the final outcome in Eq. (7). Eq. (7) predicts a T_r - $VPD^{1/2}$ scaling instead of T_r - VPD scaling (i.e., Dalton's law) but the linear scaling emerges when setting C_i/C_a to a constant. As discussed elsewhere (Katul et al., 2010), the T_r - $VPD^{1/2}$scaling is an emergent outcome of the optimization theory for all C3 plants and is not an outcome of any model calibration or empirical fit to gas exchange measurements. Detailed optimality theories that resolve all the non-linearities in the biochemical demand function have also been derived but their performance is commensurate with outcomes such as Eq. (6) (Katul et al., 2010; Volpe et al., 2011).

The compensation point is assumed to vary only with air temperature (T_a) and is calculated using standard equations (Sellers et al., 1996),

$$\Gamma=\frac{5O_2}{2600\times 0.57^{\frac{T_a-25}{10}}} \tag{8}$$

where O_2 (Pa) is the leaf interior partial O_2 pressure treated as a constant set to 2.09 × 10^4 Pa (Sellers et al., 1992). Inserting Eq. (8) into Eq. (7) and converting the unit of T_r from mol m^{-2} s^{-1} to W m^{-2} using the latent heat of vaporization (=2.45 × 10^6 J kg^{-1}), an expression for T_r can be derived and is given as,

$$T_r=\frac{44.10(\alpha \mathrm{SIF}+\beta)\bullet\sqrt{1.6\lambda_{cf}}}{\sqrt{P_a\left(C_a-\frac{5O_2}{2600\times 0.57^{\frac{T_a-25}{10}}}\right)}}\mathrm{VPD}^{1/2} \tag{9}$$

At first glance, Eq. (9) appears to be independent of LAI though the effects of LAI are implicit in the coefficients α and β together with the SIF signal. The λ_{cf} is assumed to be stationary over time for most plant species (Lloyd and Farquhar, 1994). Values from published gas exchange studies are used in Eq. (9) (Lloyd and Farquhar, 1994, see Table S1 in the supplementary information).

Before proceeding further, several points must be raised when invoking a constant λ_{cf}. It is now established that λ_{cf} can vary with progressive hydraulic limitations and/or large changes in atmospheric CO_2 concentration as discussed elsewhere (Ellsworth et al., 1995; Manzoni et al., 2011; Manzoni et al., 2013; Mrad et al., 2019). Eq. (6) shows that holding λ_{cf} constant while increasing C_a results in an increase in C_i/C_a not congruent with stable isotope measurements at Free Air CO_2 Enrichment experiments that predict a near-constant C_i/C_a independent of C_a (Ellsworth et al., 1995). As such, λ_{cf} should scale with $1/C_a$ as discussed elsewhere (Katul et al., 2010) and as theoretically argued using dynamic optimality theories (Manzoni et al., 2013). However, to keep the number of parameters to a minimum for global ET estimates, it is assumed that C_a did not change appreciably over the calibration period so as to justify its inclusion as a modifier for λ_{cf}. Moreover, T_r scales sub-linearly with λ_{cf} (i.e., $T_r \sim \sqrt{1.6\lambda_{cf}}$) and small modifications to λ_{cf} due to minor increases in C_a have minimal impact on T_r.

With regards to soil evaporation, the E_s formulation used in prior work (Zhou et al., 2022) is used. This formulation employed the surface available energy and relative humidity complemented with vegetation properties (Leaf Area Index). This formulation is given by (Yan et al., 2012),

$$E_s=1.35RH\frac{\Delta(R_n-G)e^{-k_A LAI}}{\Delta+\gamma} \tag{10}$$

where RH (no unit) is the mean air relative humidity, Δ is the slope of saturation vapor pressure - air temperature curve, γ is the psychrometric constant, R_n is net radiation above the canopy, G is the ground heat flux and is neglected relative to R_n, and a plausibility argument is that at a 4 day timescale, the temporal value of G is near-zero. Excluding G can bring about some uncertainty, but the overall effect should be minimum given that G usually accounts for under 6% of R_n when evaluated by using FLUXNET sites (data not shown). The k_A here is the light extinction coefficient and the synthesized values by Zhang et al. (2014b) are adopted in this study. In particular, the value is 0.62 for croplands, 0.59 for broadleaf forests (evergreen broadleaf & deciduous broadleaf & mixed forests), 0.45 for needleleaf forests (evergreen & deciduous needleleaf forests), 0.56 for shrublands (open and closed shrublands), and 0.50 for grasslands (grasslands & savannas); the mean value of 0.56 of all ecosystems in the study by Zhang et al. (2014b) is adopted for cropland/natural vegetation mosaic and wetlands in this study; LAI is leaf area index (m^2 m^{-2}). When combining Eqs. (9) and (10), the modeled transpiration and soil evaporation can be combined and expressed as,

$$T_r+E_s=\frac{44.10\ (\alpha \mathrm{SIF}+\beta)\bullet\sqrt{1.6\lambda_{cf}}}{\sqrt{P_a\left(C_a-\frac{5O_2}{2600\times 0.57^{\frac{T_a-25}{10}}}\right)}}\mathrm{VPD}^{1/2}+1.35RH\frac{\Delta(R_n-G)\bullet e^{-k_A LAI}}{\Delta+\gamma} \tag{11}$$

Here, the T_r + E_s part has only two 'free' parameters - α and β that must be externally calibrated for each site. Also, it is noted that $\sqrt{1.6\lambda_{cf}}$ multiplies α and β – and hence – it cannot be readily disentangled from them if treated as a third fitting parameter. The conversion factor of 44.10 for the T_r expression is to ensure these fluxes are in units of W m^{-2}.

The α and β parameters were calibrated at FLUXNET sites during dry periods with rainfall events excluded (see 2.2).

The evaporation of canopy intercepted water was calculated using a modified analytical model (Gash, 1979; Gash et al., 1995). Here, the canopy and the trunk are assumed to be the entire interception surface so as to simplify the calculation. Remote sensing data are used to calculate the global canopy intercepted evaporation (Zheng and Jia, 2019). The Gash model describes the volume of water that is intercepted by the canopy, and the intercepted water is considered as the interception re-evaporation. The intercepted water is calculated as,

$$E_i = \begin{cases} c \bullet P_G \; P_G \le P_G^{'} \\ c \bullet P_G^{'} + c \bullet \dfrac{\bar{E}}{\bar{R}} \bullet \left(P_G - P_G^{'}\right) \; P_G > P_G^{'} \end{cases} \tag{12}$$

where c is the canopy cover fraction evaluated using $1 - e^{-k_A LAI}$ (Zheng and Jia, 2019), and k_A is the light extinction coefficient as aforementioned and the same parameterization is adopted (Zhang et al., 2014b); $\bar{R}$ (mm hr^{-1}) denotes the mean rainfall rate which can be directly evaluated by using the rainfall records, and $\bar{E}$ (mm hr^{-1}) denotes the mean evaporation rate during rainfall and can be evaluated by using a Dalton type evaporation equation where the evaporation rate is driven by water vapor concentration gradient between the canopy surface and the air; note that both $\bar{R}$ and $\bar{E}$ are evaluated for certain fixed periods (e.g., 1 month, 2 months, among others); P_G (mm) is the gross rainfall for each rainfall event; $P_G^{'}$ (mm) is the rainfall threshold for saturating the canopy and can be evaluated as

$$P_G^{'} = -\frac{\bar{R}}{\bar{E}} \bullet \frac{S_{veg}}{c} \bullet ln\left(1 - \frac{\bar{E}}{\bar{R}}\right) \tag{13}$$

where S_{veg} denotes the vegetation canopy storage capacity (mm) and can be evaluated as,

$$S_{veg} = S_v \bullet VAI \tag{14}$$

where S_v (mm) is the specific storage capacity (see Cui et al., 2015). The VAI (m^2 m^{-2}) is the vegetation area index approximated by using LAI and the area index of dead leaves, branches, stem and trunk, L_s (m^2 m^{-2}),

$$VAI = LAI + L_s \tag{15}$$

where L_s varies with LAI and can be quantified as,

$$L_s^n = max\left\{\left[\varepsilon \bullet L_s^{n-1} + max\left(LAI^{n-1} - LAI^{n}, 0\right)\right], L_{s,min}\right\} \tag{16}$$

Here, L_s^n and L_s^{n-1} denote the n^{th} and $(n-1)^{th}$ L_s of the time series, respectively, and $L_{s,\,min}$ is the minimum value of L_s; LAI^n and LAI^{n-1} denote the n^{th} and $(n-1)^{th}$ green LAI of the time series, respectively; ε denotes the left rate of residuals and 1-ε denotes the removal rate. The parameterizations of $L_{s,\,min}$ and ε are taken from Cui et al. (2015). The unit of E_i was ultimately converted to W m^{-2} using latent heat of vaporization ($=2.45 \times 10^6$ J kg^{-1}).

2.2. Deriving the α and β parameters over the globe

The contiguous SIF product (CSIF) is used (Zhang et al., 2018) to constrain transpiration and the model parameters α and β are calibrated against latent heat flux measurements reported by the FLUXNET2015 dataset (http://fluxnet.fluxdata.org/data/fluxnet2015-dataset/). CSIF was produced using a machine learning algorithm trained using the Orbiting Carbon Observatory-2 (OCO-2) SIF measurements and the MODIS reflectance product. The CSIF employed here has a spatial resolution of 0.05°at the 4-day temporal resolution from January 2000 to December 2018. The FLUXNET site is paired with CSIF pixel in which the meteorological tower resides and the parameters of the models were optimized at the flux site level.

FLUXNET2015 is a worldwide network of eddy-covariance turbulent flux measuring stations, which include near-surface fluxes of carbon dioxide, water vapor, and energy (Pastorello et al., 2020). For each site, the following variables were selected in the parameter determination: latent heat flux (W m^{-2}), VPD (kPa), C_a (in ppm), net radiation (W m^{-2}), air temperature (in °C), and air relative humidity (unitless). Inconsistency usually exists between the flux tower footprint (usually 3 to 5 km^2) and remotely sensed SIF coverage due to land heterogeneity. We used Net Difference Vegetation Index (NDVI) to select sites satisfying the following two requirements: (1) The maximum, minimum, and standard deviation of NDVI (MOD13Q1) of the grid point in which the site is located is within 20% of the difference of the corresponding statistical index of the adjacent area (5×5 km^2 area in the center of which the flux site is located); (2) The maximum of NDVI of the target grid point must be >0.2 to exclude the sites with barren land in the growing season (see Zhou et al., 2022). Here the growing season is determined by using 50% thresholds of annual SIF data series, in particular, the spring onset is determined by 50% of the annual maximum of SIF, and the last fall day is defined as the date when the seasonal SIF drops to 50% of the annual maximum (Jeong et al., 2017). Sites with temporal coverage longer than 2 years are included in the analysis. These selection criteria resulted in 68 flux sites (Table S2) for parameter calibration, and the sites covered all land types under the IGBP land classification except for deciduous needleleaf forest (DNF), cropland/natural vegetation mosaic (CVM), water bodies (WAT) and urban and built-up land (URB). The land use types of water bodies and urban and built-up were not considered here. The temporal resolution of all flux site variables was aggregated to 4 days to be consistent with that of the CSIF data. To reduce uncertainty, we removed data when the meteorological variables over the 4 days' period missed >10% data. The model parameters α and β were calibrated at the site level using the least square method and later employed to derive the global distribution based on the IGBP vegetation type classification. Here, the MODIS product MCD12C1 was used for global vegetation distribution, which has a spatial resolution of 0.05° (See Fig. S1).

The parameters of α and β describe the relation between GPP and SIF, where α represents the ratio of light use efficiency to fluorescence yield (Yang et al., 2015) and β is the intercept of this relation. Thus, any factor that influences light use efficiency and fluorescence yield affect these parameters. Vegetation type, canopy structure, meteorological conditions impact these two parameters as well (e.g., Pierrat et al., 2022). In constructing the spatial distribution of these two parameters, we only considered the vegetation type by using global plant functional type (PFT) and the environmental variables of mean annual precipitation (MAP), mean annual temperature (MAT) and Dryness Index (DI). The parameters of α and β were first calibrated at the 68 FLUXNET sites, and then two methods were used to determine the spatial distribution of these parameters over the terrestrial globe using PFT as follows:

(1) Mean value model:

For PFTs with limited number of sites ($0 < N < 5$) including Closed Shrublands (CSH), Deciduous Broadleaf Forests (DBF), Mixed Forests (MF), Open Shrublands (OSH) and Wetlands (WET), a PFT-based mean value approach similar to the parameterization method commonly used in land surface models is used and given as

$$y_i^j = c^j + \delta_i \tag{17}$$

where y_i^j is the value of the parameter α or β at the i^{th} flux station in the j^{th} PFT, c^j is the average of the parameter of all flux stations in the j^{th} PFT, and δ_i is the error.

(2) Regression model:

For PFTs with at least 5 available sites, a regression model was

employed to construct the global distribution of the model parameters, including Cropland (CRO), Grassland (GRA), Evergreen Needleleaf Forest (ENF), Deciduous Broadleaf Forest (EBF), Savannas (SAV), and Woody Savannas (WSA) (See Table S3 for the 58 sites). The regression model was developed by correlating the parameters with environmental variables for each PFT as,

$$y_i^j = \left(n^j\right)^T X_i + \delta_i \tag{18}$$

Here, $(n^j)^T$ is the regression coefficient matrix for the j^{th} plant functional type. The X_i is the matrix of selected environmental variables of the i^{th} flux site. The environmental variables here include MAT, MAP, and Dryness Index (DI) evaluated as the ratio of Potential Evapotranspiration (PET) and MAP, all of which are factors that commonly control local climate, as well as photosynthesis and plant transpiration. At the FLUXNET sites, MAT and MAP were obtained by averaging long-term precipitation and temperature records available in the FLUXNET2015 datasets, where the site DI was evaluated and the PET was calculated by using Priestley-Taylor model (Fisher et al., 2008; Zhang et al., 2019; Liu et al., 2022).

The global distribution of MAT and MAP were obtained as long-term averages of ERA5 temperature and precipitation records. Since the magnitude of land precipitation is usually below 3000 mm yr^{-1} in most areas, extreme precipitation records (>3000 mm yr^{-1}) were replaced by 3000 mm yr^{-1}. The global distribution of DI was calculated using MAP and PET estimated from the Priestley-Taylor model (see Fisher et al., 2008; Purdy et al., 2018 for details). The global distribution of model parameters was determined using either the mean value model or the regression model with MAT, MAP and DI. For those PFTs with limited sites, the mean value of the parameters of the PFT was used; for the DNF and CVM PFTs, as no flux sites were available to calibrate the parameters, we used the average of the site-calibrated parameters of ENF for DNF, and the average of CRO for CVM.

2.3. Drivers of the global ET model

Meteorological input from the ERA5 terrestrial meteorological reanalysis data (https://cds.climate.copernicus.eu/) was used to drive the ET calculations. ERA5-Land is the latest generation of meteorological reanalysis data operated by the European Centre for Medium-Range Weather Forecasts (ECMWF) (Hersbach et al., 2020). Covering all conventional meteorological data from 1950 to the present, it assimilates remote sensing products, surface and upper atmosphere meteorological data, including different regions of the globe with varying time scales. We used the hourly meteorological variables at a spatial resolution of 0.1°, including air temperature (T_a, °C), dew point temperature (T_{dew}, °C), net short-wave radiation and net long-wave radiation (W m^{-2}). The VPD was calculated as

$$VPD = e_{sat} - e_a \tag{19}$$

where e_{sat} (kPa) is the saturation vapor pressure and e_a (kPa) is the actual water vapor pressure derived using T_{dew}.

Because most plant photosynthesis occurs during daytime, we averaged the meteorological records between 06:00 and 18:00 local time to the 4-day window. Such treatment brings about some uncertainty to nighttime evaporation. However, the effect should be low as nighttime evaporation accounts for 6% of the total ET on average as evaluated using the original latent heat flux measurements provided by FLUXNET2015 database (data not shown). These estimates also match other reported nighttime ET estimates in the literature (Novick et al., 2009). To match the resolution of the SIF data, we resampled the ERA5 radiation data from 0.1° to 0.05° using a spline function interpolation.

Leaf area index (LAI) was obtained from the MODIS leaf area index product (MCD15A3H V006) for the period 2003–2018 to support the E_s calculations in Eq. (10) and the canopy interception evaluations. This LAI product has a spatial resolution of 500 m and a temporal resolution of 4 days. At the stage of site parameter calibration, the LAI grid points were extracted to match the flux sites. For global ET calculations, the global LAI was aggregated to 0.05° to match the spatial resolution of the SIF data. To conceptualize the global ET estimation procedure, Fig. 1 features a flowchart highlighting the key variables used and their resolution.

The global precipitation dataset MSWEP (Beck et al., 2019) was used to drive the Gash model for global E_i estimates. The MSWEP dataset has a spatial resolution of 0.1° and a temporal resolution of 3 h by optimally merging multiple data sources ranging from gauge measurements, satellite observation, to reanalysis production. The high quality of MSWEP guarantees the quality of the canopy interception evaporation estimate. Before running the Gash model, the mean rainfall rate ($\bar{R}$) was evaluated using the original 3-hourly data for every 28 day-window (i.e., 7 × 4-day windows of the calculation step of ET), then the Gash model was run at the daily time step that was finally aggregated to 4 days to agree with other ET component calculations. To match the spatial resolution of 0.05° for the transpiration and soil evaporation estimates, the four 0.05° pixels within the 0.1° pixel directly adopted the corresponding interception evaporation value.

2.4. Global evapotranspiration products used for comparison

Three widely used meteorologically-driven global ET products were used for comparisons with the proposed ET_{SIF}. The first product is the GLEAM ET data (Martens et al., 2017). GLEAM calculates PET using the Priestley-Taylor equation (Priestley and Taylor, 1972) with observed surface available energy and surface temperature. GLEAM estimates actual ET by imposing a constraint on PET. In particular, GLEAM combines observations of Vegetation Optical Depth (VOD) and estimates of root-soil moisture that impose ET limitations using an empirical reduction factor. Different from other ET products used for comparisons in this study, GLEAM explicitly considers snow sublimation. The GLEAM ET data has a spatial resolution of 0.25° and a temporal resolution of 1 day.

The second ET product is derived from the PT-JPL model (Fisher et al., 2008) that employs the Priestley-Taylor formulation assumed to represent PET (Priestley and Taylor, 1972). The PT-JPL model then employs multiple constraints to convert the corresponding PET into actual canopy transpiration, canopy interception evaporation and soil evaporation. The constraints for canopy transpiration include leaf area index, green fraction of the canopy, plant temperature and plant moisture; the constraint for soil evaporation is evaluated using relative humidity and vapor pressure deficit; the constraint for the interception evaporation is defined as the fraction of time when the surface is wet evaluated using relative humidity. The model description is featured elsewhere (Fisher et al., 2008) and is not repeated here. Unlike GLEAM, all the model parameters of PT-JPL are preset, thus no calibration is needed when using the model. The PT-JPL model is run on monthly timescales and these monthly ET estimates from 2003 to 2018 at spatial resolution of 36 km (or 0.25°) are used for comparison with the proposed ET_{SIF}.

The third ET product is the land MOD16, which was derived by Mu et al. (2007, 2011) using a modified Penman-Monteith equation with parameterized stomatal conductance formulation. The dataset is built on MODIS-reported land cover, albedo, LAI, meteorological forcings, etc. Note that MOD16 only evaluates ET over vegetated areas, and all sparsely vegetated or non-vegetated areas are left as blank. The MOD16 has a spatial resolution of 500 m and a temporal resolution of 8 days.

When comparing the proposed ET_{SIF} with the three products with varying spatial and temporal resolutions, the finer-resolution datasets were aggregated to agree with the lower-resolution ones.

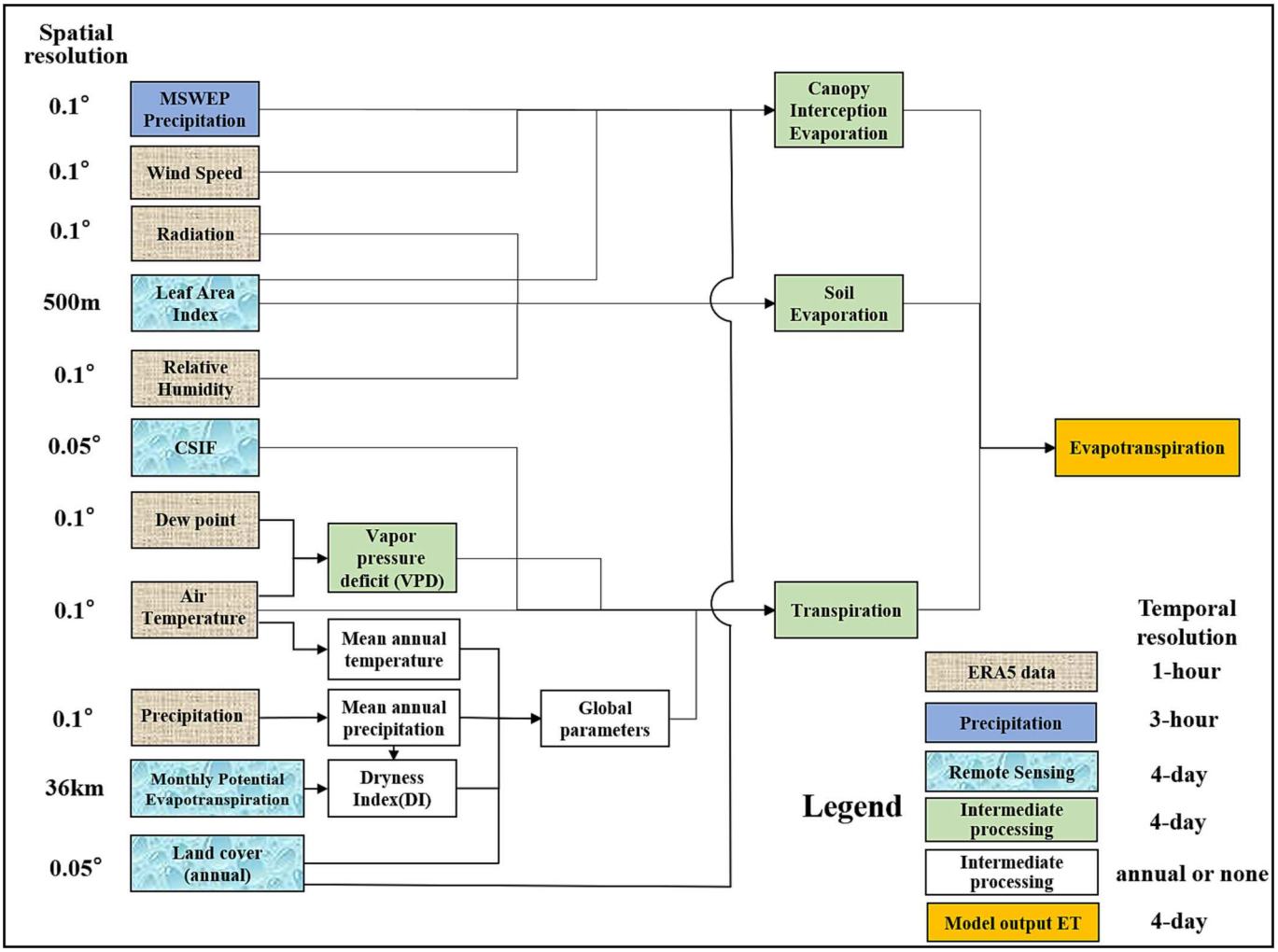

Fig. 1. Flowchart of the ET model (labeled as ET_{SIF}) calculations featuring the differing inputs and outputs along with their associated time scale. The spatial resolutions of the original inputs are listed on the left and all the variables during the intermediate processing are at 0.05° resolution. The ERA5 precipitation record is used when deriving the dryness index (DI).

3. Results

3.1. Calibrating parameter at flux site level and constructing the parameters over the globe

The α and β were calibrated for each of the 68 sites from the FLUXNET2015 dataset. The ET_{SIF} model-data comparisons were not independent of PFTs as shown in Fig. 2. The performance of the ET_{SIF} model is also presented for the selected site for each PFT (see Fig. S2). In particular, R^2 of the calibration is higher than 0.50 for 53 sites, and higher than 0.70 for 34 sites; however, R^2 at some sites are low and fall in the range of 0.1–0.3. The low R^2 was mainly at CSH, EBF and SAV sites. The model parameters are featured by PFTs in Fig. 3. The parameters are statistically uniform across sites for some of the PFTs (i.e., MF, WSA, SAV, EBF, DBF), whereas they showed variability for other PFTs (i.e., ENF, SAV, CRO, OSH, CSH). In particular, α of ENF showed substantial variability among different sites. For those PFTs with limited sites ($N < 5$), the average of the parameters from available sites were employed (Table 1). For PFTs with at least 5 sites, a multiple linear regression model was used to relate α and β to MAP, MAT and DI (Fig. 4; Table 1). For most PFTs, the multiple linear regression captures the variability of parameters among different sites ($R^2 = 0.6$–0.8); but for PFTs such as DBF and GRA, the performance was poor with $R^2 < 0.3$. Given that the value of $R^2 > 0.1$, the climatic and environmental variables of MAP, MAT and DI are used in the regression model to determine α and β in lieu of using an ad-hoc mean values set by a PFT. Therefore, the regression model was used for each of the 6 PFTs to produce the global distribution of α and β (Fig. 5). Note that the lower boundary of β was artificially set to 0 when estimating the global ET to avoid negative values of photosynthesis and transpiration due to the false parameters on a 4-day interval. We tested setting $\beta = 0$ when calibrating the parameters at flux sites and found the overall performances showed no discernible difference (See Table S2). The constructed spatial distribution of α showed clear lower values over tropical area (~10–20 $\mu mol\ m^{-2}\ s^{-1}/mW\,m^{-2}nm^{-1}sr^{-1}$) and higher values over the boreal forests (~50–70 $\mu mol\ m^{-2}\ s^{-1}/mW\,m^{-2}nm^{-1}sr^{-1}$). On the contrary, the parameter β showed high values over the tropical area (~4–8 $\mu mol\ m^{-2}\ s^{-1}$).

3.2. The distribution of global ET from 2003 through 2018

The global ET_{SIF} was produced from 2003 through 2018 and spatial maps of the annual means are featured in Fig. 6. Globally, mean annual ET_{SIF} ranged from 0 to 150 W m^{-2} (Fig. 6). The higher values were in eastern North America, South America, South Africa, Southeast Asia, Southern China, and part of Australia. The mean annual ET_{SIF} in most part of the Amazon forest region ranged from 100 to 150 W m^{-2}, while in most African regions except for the Sahara Desert and the dry climate

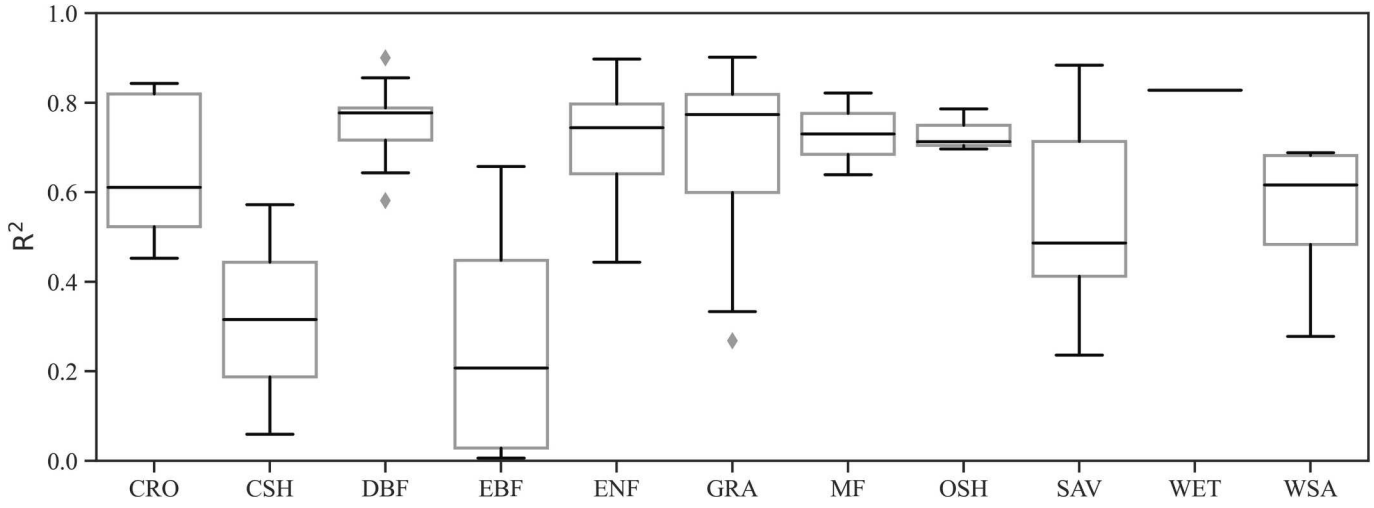

Fig. 2. The coefficient of determination (R^2) of the ET_{SIF} model in reproducing the measured evapotranspiration (ET) for each of the IGBP plant functional types (PFTs).

Fig. S2 features examples for flux sites when calibrating the model. Hereafter for the boxplot, the central line denotes the median; the upper whisker is the maximum value of the data that is within 1.5 times the IQR over the 75% percentile, and the lower whisker is the minimum value of the data that is within 1.5 times the IQR under the 25% percentile, note that the interquartile range (IQR) here is defined as the difference between the 75% and 25% percentiles; the diamond points denote outliers falling beyond the range [25% percentile-1.5*IQR, 75% percentile+1.5*IQR]. The IGBP code is: CRO-Croplands, CSH-Closed Shrublands, DBF-Deciduous Broadleaf Forests, EBF-Evergreen Broadleaf Forests, ENF-Evergreen Needleleaf Forests, GRA-Grasslands, MF-Mixed Forests, OSH-Open Shrublands, SAV- Savannas, WET-Wetlands, WSA-Woody Savannas.

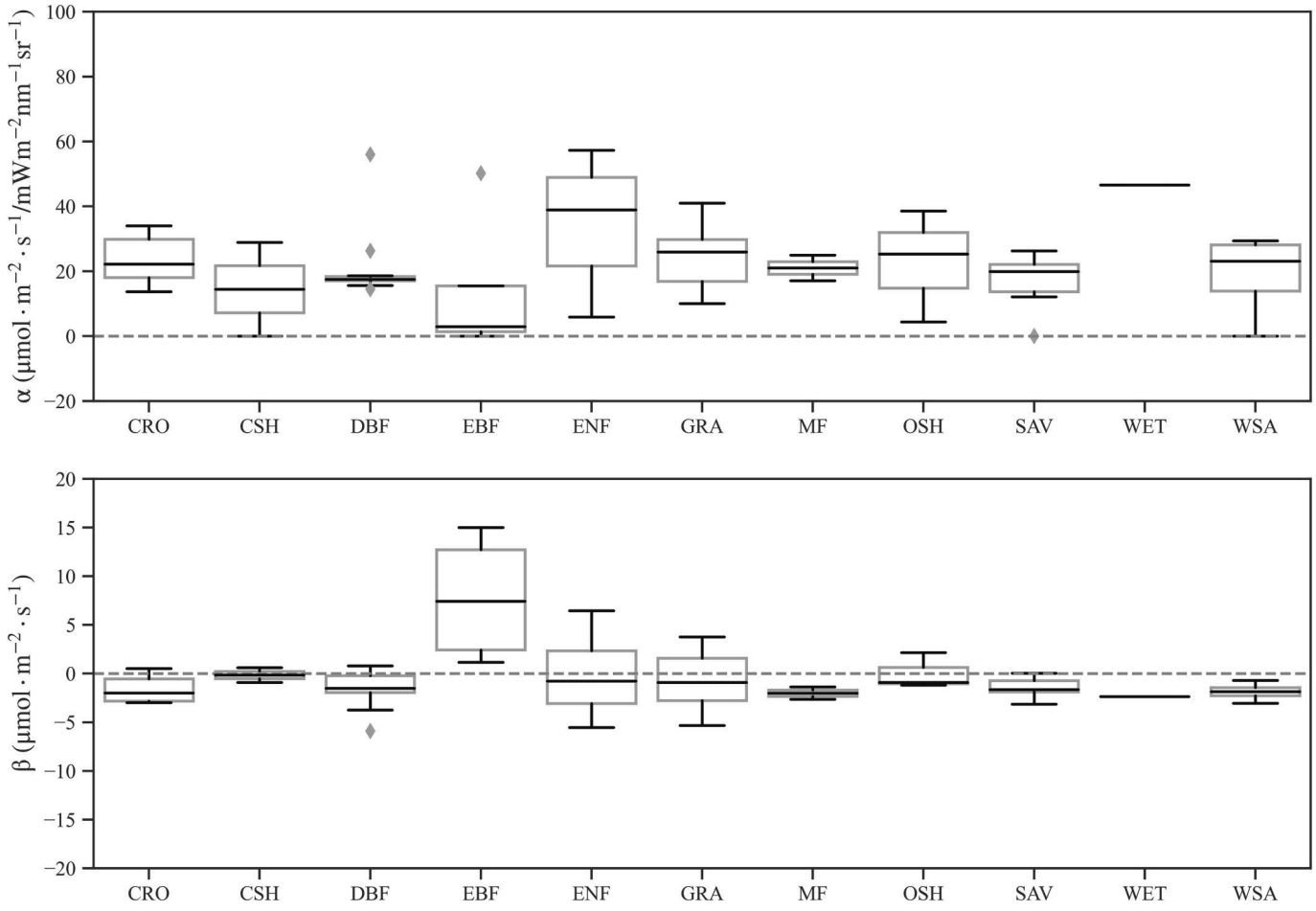

Fig. 3. Variability of the parameters α (μmol m^{-2} s^{-1}/mW m^{-2} nm^{-1} sr^{-1}) and β (μmol m^{-2} s^{-1}) across different plant functional types (PFTs).

Table 1
Mean value for plant functional types with limited sites (N < 5) and the regression relation of parameters for plant functional types with sufficient sites ($N \geq 5$) derived from calibration over FLUXNET sites.

PFT	α	β
CSH	14.46	−0.15
EBF	14.00	7.75
MF	21.03	−2.01
OSH	22.75	0.02
WET	46.61	−2.36
DNF	35.14	−0.37
CVM	23.61	−1.61
CRO	9.86 + 0.047 MAP–0.170 MAT+2.733 DI	6.21–0.008 MAP–0.170 MAT–0.108 DI
DBF	33.31–0.014 MAP–3.048 MAT+29.886 DI	0.54–0.002 MAP+0.575 MAT–6.352 DI
ENF	37.32–0.009 MAP–0.665 MAT+6.582 DI	−4.09 + 0.004 MAP+0.214 MAT–0.844 DI
GRA	12.17 + 0.009 MAP+0.444 MAT–0.117 DI	−0.77 + 0.004 MAP–0.321 MAT+0.738 DI
SAV	87.11–0.050 MAP+0.561 MAT–16.232 DI	−11.38 + 0.005 MAP+0.104 MAT+1.418 DI
WSA	184.77–0.0045 MAP–4.06 MAT–33.15 DI	−15.79–0.0012 MAP+0.325 MAT+2.69 DI

Note that the negative values of β were set to 0 when estimating the global ET, thus here the values and equations were a direct result of site calibration.

of South Africa, the mean annual ET_{SIF} >75 W m^{-2}. The ET_{SIF} can be higher than 125 W m^{-2} for some regions in central Africa and some parts of the Amazon forest. The U.S. Corn Belt and the eastern U.S. also have relatively higher ET_{SIF} (>100 W m^{-2}) resulting from cropland irrigation and intense crop agriculture. Similar ET_{SIF} values were computed for North America, North and South China where large amounts of croplands are available. In sparsely vegetated regions and drier regions such as the western United States, the Middle East, North Africa, and at higher latitudes, ET_{SIF} was lower, typically <50 W m^{-2}. The global annual ET/R_n ratio (Fig. S3) showed that ET was mostly dominated by radiation in tropical area (i.e., Amazon forest, Central Africa, Southeast Asia) and intensely irrigated area (e.g., Midwest of U.S., India, North part of China) with a higher ET/R_n ratio, while in the arid region (e.g., North Africa, Middle East, Northwestern China) ET was mostly dominated by water availability with a lower ET/R_n ratio. The maximum and minimum 4-day averaged ET_{SIF} are shown in Fig. S4, and a maximum of about 500 W m^{-2} appeared at higher latitudes of Eurasia, Southeastern China, India, part of the Amazon forest, Mideast U.S.. The minima in the tropical area exceed 50 W m^{-2}.

Monthly averaged global ET_{SIF} was also computed and seasonal variations across the whole globe evaluated (Fig. 7) to assess controls of leaf area dynamics on ET. For the Northern Hemisphere spring (Fig. 7a-c), ET_{SIF} was low in Northern China, Southern China, Eastern U.S., and across Europe as vegetation greening commences. At the same time, ET_{SIF} remained high in South America along the Amazon rainforest and southern South America, Indonesia and Congo. In the Northern Hemisphere summer (Fig. 7d-f), the ET_{SIF} reached a peak, especially in the Eastern U.S., Northern and Southern China, and Europe, where ET_{SIF} as high as 150 W m^{-2} was computed. In the Amazon forest, ET_{SIF} remained high during the spring. In southern South America, overall ET_{SIF} was low as the southern hemisphere entered winter at this time. Similarly for the southern part of South America, the overall ET_{SIF} in Australia was also low due to the winter season. As the Northern Hemisphere approached fall (Fig. 7g-i), ET_{SIF} began to decline in North America, most parts of Europe, northern China, and southern China. Near the U.S. Corn belt,

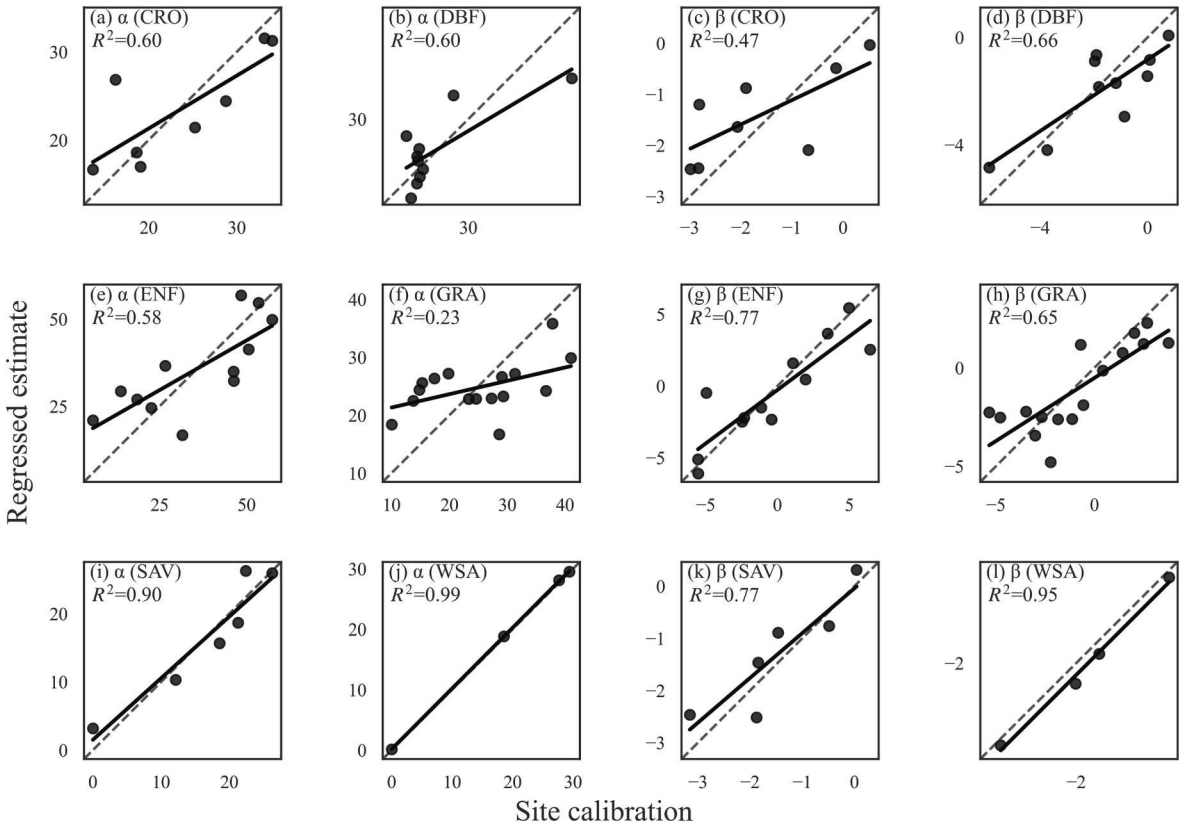

Fig. 4. Performance of the multiple linear regression model to explain variability in α (μmol m^{-2} s^{-1}/mW m^{-2} nm^{-1} sr^{-1}) and β (μmol m^{-2} s^{-1}) for different plant functional types.
Note that the x axis represents the parameters of site calibration and the y axis represents the estimate when using the multiple linear regression with Mean Annual Temperature (MAT), Mean Annual Precipitation (MAP) and Dryness Index (DI).

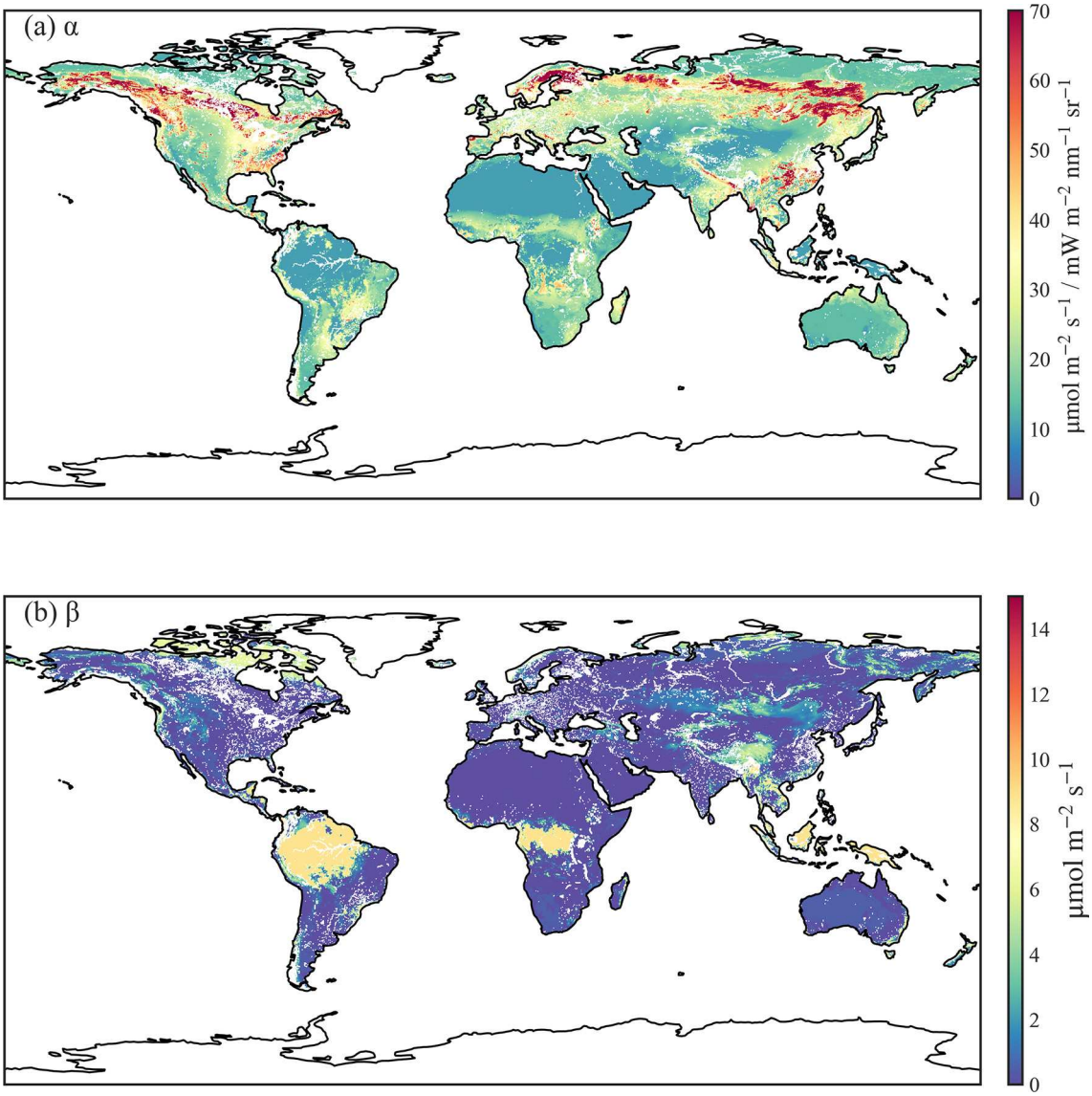

Fig. 5. Global distribution of the model parameters α (a) and β (b) used in ET_{SIF}. The β = 0 was externally imposed to ensure no negative GPP occurs when SIF = 0 over a 4-day averaging interval.

ET_{SIF} dropped from over 150 W m^{-2} in the summer to about 50 W m^{-2}. In Europe, ET_{SIF} dropped from about 100 W m^{-2} in summer to about 25 W m^{-2}. In China, the overall ET_{SIF} dropped to about 100 W m^{-2}. As the southern hemisphere entered spring, ET_{SIF} increased to about 100 W m^{-2} in most parts of South America and Australia. The Amazon rainforest and parts of Southeast Asia still maintained high ET_{SIF} due to low seasonal variations in this region. In the Northern Hemisphere winter (Fig. 7j-l), ET_{SIF} remained low in North America, Europe, and China. In the Amazon rainforest and Southeast Asia, ET_{SIF} remained relatively high throughout the year. As summer progressed in the Southern Hemisphere, the overall ET_{SIF} remained high for all parts of Australia and southern South America. The lower coefficient of variation (CV) of ET_{SIF} in the tropical area implies that ET is generally stable all year round, and the higher CV in the higher latitude of the Northern Hemisphere and the arid area (Northern Africa, Middle East) implies that the ET is subject to high seasonal variation (Fig. S5). To sum up, the overall spatial and temporal patterns of global ET_{SIF} appear consistent with logical expectations. It must be underscored that LAI data product did not enter into the transpiration calculations explicitly and was only used in the soil- and intercepted water evaporation.

To reveal other patterns, ET_{SIF} was averaged by latitude and the seasonal variation of latitudinal ET_{SIF} is evaluated and featured in Fig. 8 (a). As expected, near the equator, ET_{SIF} showed minor seasonal variations with a relatively high ET_{SIF} level across seasons. In the northern and southern hemispheres, ET_{SIF} was higher in the plants' active season compared to the dormant season as expected. Global ET_{SIF} also showed a minor increasing trend (0.257 mm yr^{-1}) over the 2003–2018 period though this trend was not statistically significant at the 95% confidence level (Fig. 8b).

4. Discussion

4.1. Comparison with other ET products

Using global SIF products complemented with meteorological inputs and land cover properties, a new global ET_{SIF} product for the period of 2003–2018 was developed and compared to prior global ET products. The global distribution of ET_{SIF} derived here are comparable with other common meteorologically-driven ET products of GLEAM, PT-JPL model and MOD16 though discrepancies exist as shown by the differences in Fig. 9. The differences between ET_{SIF} and prior algorithms is typically about −20 to 20 W m^{-2} (Fig. 9) – or under 0.7 mm d^{-1}. This difference is

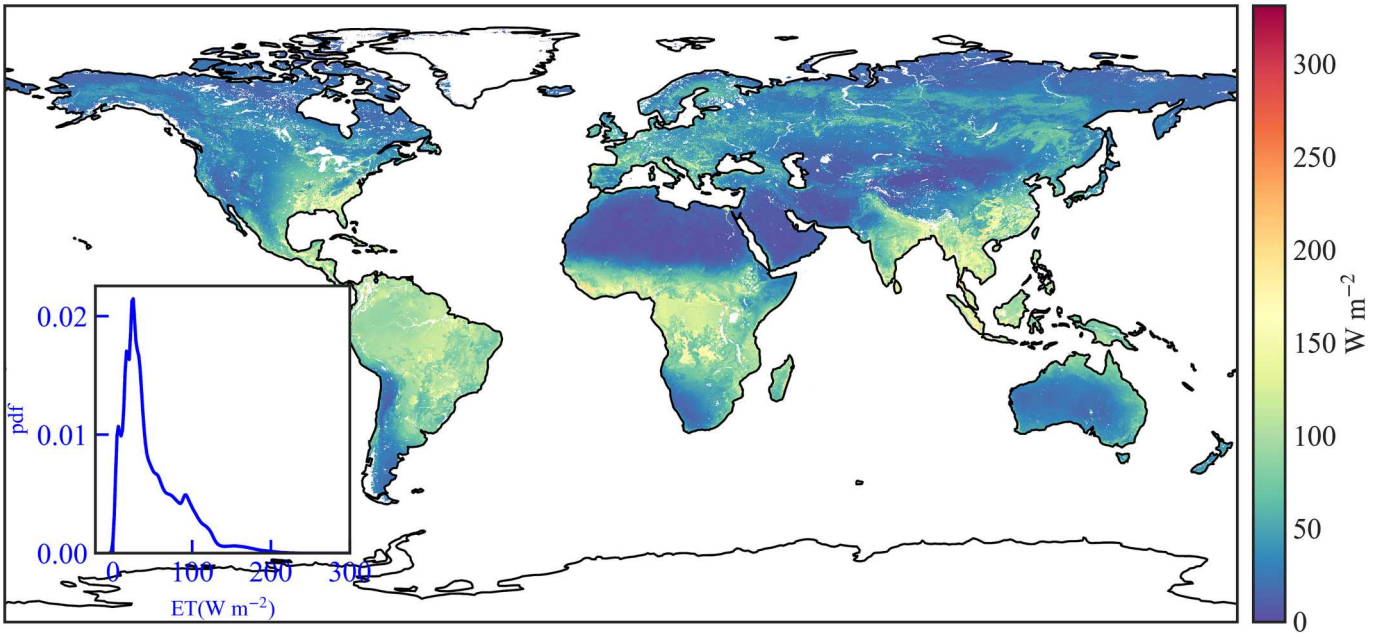

Fig. 6. Global distribution of the computed annual mean evapotranspiration (ET_{SIF}) for the study period (2003–2018); the inset panel shows the probability density function (pdf) of annual mean ET_{SIF}.

deemed acceptable given the differences in input variables and the differences in model complexities and assumptions. The proposed ET_{SIF} showed evident differences from MOD16 and a bimodal curve pattern existed in the probability density function of those differences (Fig. 9). Substantial differences between ET_{SIF} and some of the other products are found in the Amazon rainforest, some parts of central Africa and Indonesia where the rainforest is dominant as well as Eastern India, where agriculture is dominant, and in central and western Australia, part of Africa, part of South and Southeastern Asia where the estimated residuals ranged from 20 to 60 W m^{-2}. Part of the uncertainty may be related to the parameters that adopt the average of the PFTs in most regions of western Australia, Africa and part of Asia, where eddy-covariance flux sites over the major PFTs remain insufficient for accurate GPP-SIF parameterization. But the difference may also result from the limitations in other products.

The comparison between the proposed ET_{SIF} and GLEAM in Fig. 9 suggests the two ET methods agree on spatial patterns as the probability density function (pdf) of the corresponding difference is centered around 0 W m^{-2}; however, the comparisons with PT-JPL and MOD16 products imply that ET_{SIF} is significantly different. We compared these three ET products (GLEAM, PT-JPL and MOD16) and also found pronounced differences among themselves (Fig. S6). In general, for the four ET products evaluated in this study (ET_{SIF}, GLEAM, PT-JPL and MOD16), ET_{SIF} and GLEAM have similar spatial pattern with pronounced difference mainly emerging in tropical regions (e.g., Amazon forest), while PT-JPL and MOD16 agree on their spatial pattern; only GLEAM explicitly considers snow sublimation, but ET_{SIF} at high latitudes with snow cover is very close to GLEAM, implying that the omission of such component of ET_{SIF} does not impact the total ET estimate. Compared to PT-JPL and MOD16, the ET_{SIF} and GLEAM are consistently lower at high latitude in Northern Hemisphere, but are higher at sub-tropical regions (e.g., Southeast America, Southeast Asia). These differences probably result from different model structures and varying input variables among these models. As there is no direct 'measurement' of global ET, we have no basis to judge which is right and which is wrong. Thus, we note here that all global ET products, including ET_{SIF}, should be treated with caution.

The climatological zonal distributions of annual ET_{SIF} and other ET products are compared in Fig. 10 and the general patterns are similar with the highest values appearing around the equator. However, clear differences emerge for most latitudes of the globe. At latitudes between −5° and 5° (near the equator), ET_{SIF} was close to GLEAM and higher than the other two ET products, whereas between −25° and − 5° Southern Hemisphere as well as 5° and 20° Northern Hemisphere, the ET_{SIF} was higher than all three ET products. At the mid-latitude regions of the Northern Hemisphere (25°-50°), the general patterns across all products agree but with differences emerging in the magnitude. At high latitudes (50°-75°) of the Northern Hemisphere, the four ET products showed clear divergent values, indicating that ET estimation at high latitudes remains subject to high uncertainty. Around 15–25° Northern Hemisphere, ET_{SIF} together with GLEAM and PT-JPL showed pronounced deviations from MOD16 estimates (Fig. 10), which yielded higher ET values compared to the other three products. But such higher values of MOD16 at 15°-25° and 50°-75° of the Northern Hemisphere probably result from statistical biases as MOD16 ET of sparsely vegetated and non-vegetated areas (e.g., Sahara Desert and the permanent snow cover) was not evaluated (Mu et al., 2007, 2011), potentially elevating the corresponding latitudinal average because ET in these omitted areas is usually lower than the vegetated areas. The pronounced differences among the four ET products imply that estimating global ET remains challenging, especially at the higher latitudes (>60°) and the zone of 5–25° of the Northern Hemisphere (see the high Root Mean Square Difference in Fig. 10).

4.2. Advantages and limitations of the SIF-based ET model

The proposed ET_{SIF} is based on two physiological relations: (i) the GPP-SIF and (ii) an optimality hypothesis that predicts C_i/C_a as a function of vapor pressure deficit for C3 plants (but can be extended to C4 plants). Compared with other detailed vegetation-transpiration relations, no stomatal conductance models are required in ET_{SIF} and the effect of stomatal closure is indirectly captured by C_i/C_a. The optimality hypothesis requires the inverse of the marginal water use efficiency (λ_{cf}) that is related to the Lagrange multiplier of the optimality problem. We assumed the marginal water use efficiency is constant, but this quantity is regulated by the variation in the soil-plant hydraulic conductance (Anderegg et al., 2018; Wang et al., 2020), which is not considered in this study. In the case of C4 plants, an additional parameter (η) related to

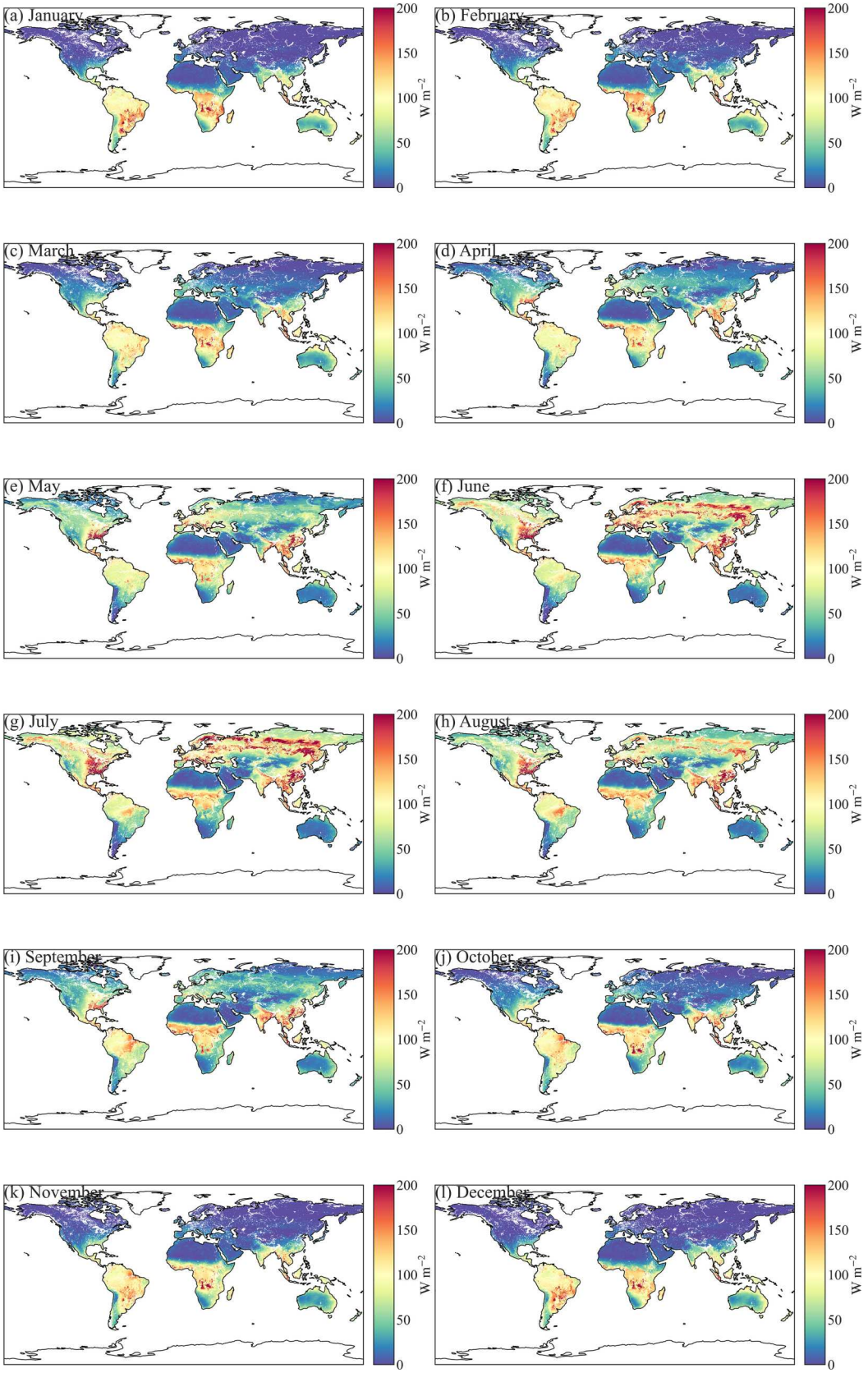

Fig. 7. Global distribution of monthly averaged evapotranspiration ET_{SIF} for the study period (2003–2018).

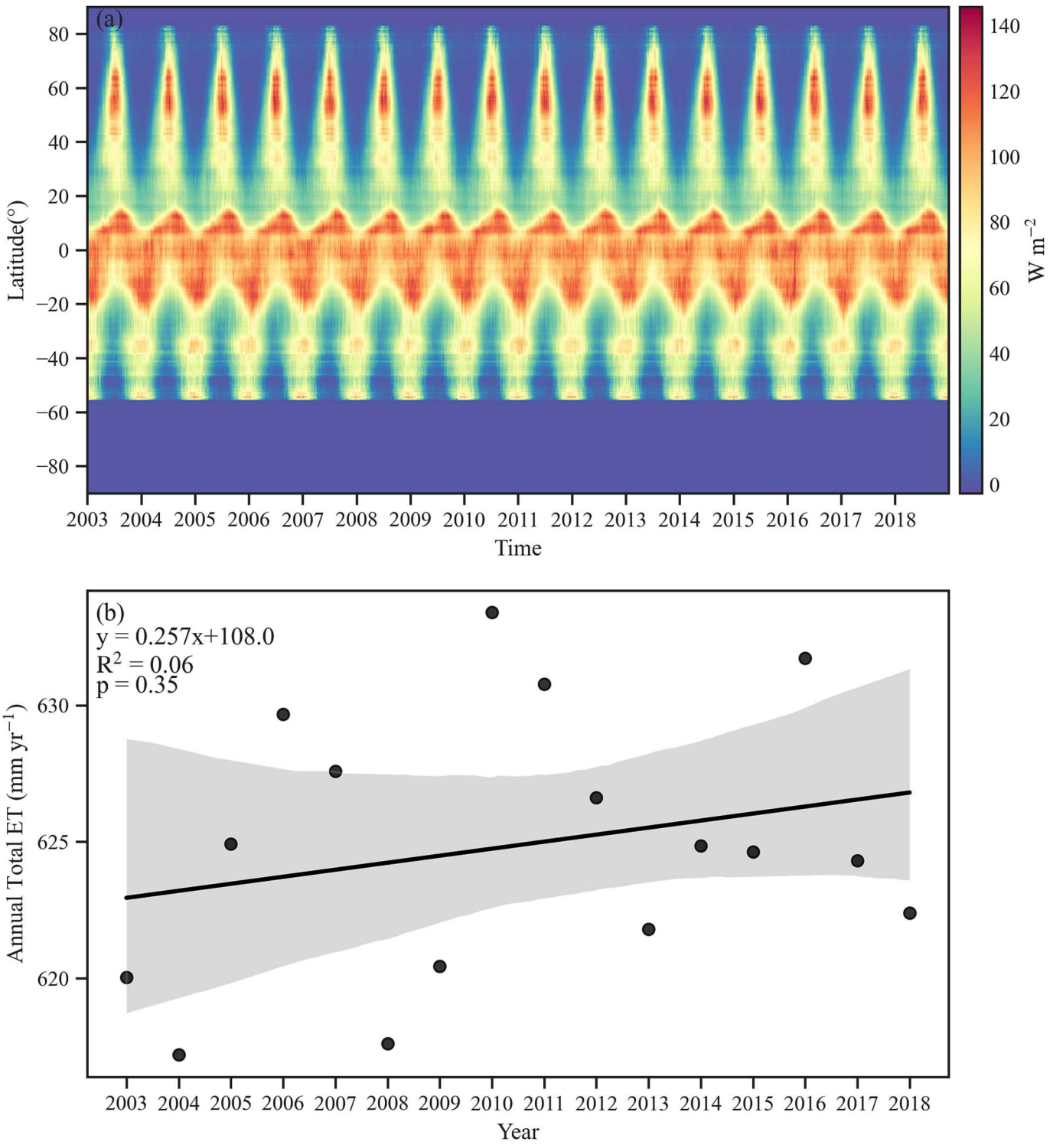

Fig. 8. Seasonal variation of latitudinal averaged evapotranspiration (ET) (a) and the temporal trend of global annual mean ET (b) over the period of 2003–2018. Note that the global annual total ET in the (b) panel has units of mm yr^{-1} for comparisons with precipitation.

the C4 pump strength is also required. ET_{SIF} developed here used λ_{cf} based on literature values and plant functional types for C3 plants. This assumption ignores hydraulic limitations and, to a lesser extent, the effects of C_a on λ_{cf}. The model calculations set $\eta = 1$ (C3 plants) even in croplands that may be occasionally dominated by corn (a C4 crop). The work here did not consider such variations in η. A partial justification for setting $\eta = 1$ over large areas and extended time periods is that corn is frequently rotated with other C3 crops (wheat or soybeans). Accounting for such rotation makes the specification of η across the globe a formidable challenge even when the numerical value of η is known. Advantages of a simplified model structure and a small number of 'free parameters' bring about potential uncertainties as well, especially in spatial upscaling. When PFT is not covered by sufficient flux measuring sites for model calibration, a mean value was adopted. The dominant PFTs in central and western Australia is OSH (Open shrublands), i.e., shrubs cover 10%–60% of the total land area in this region, but the

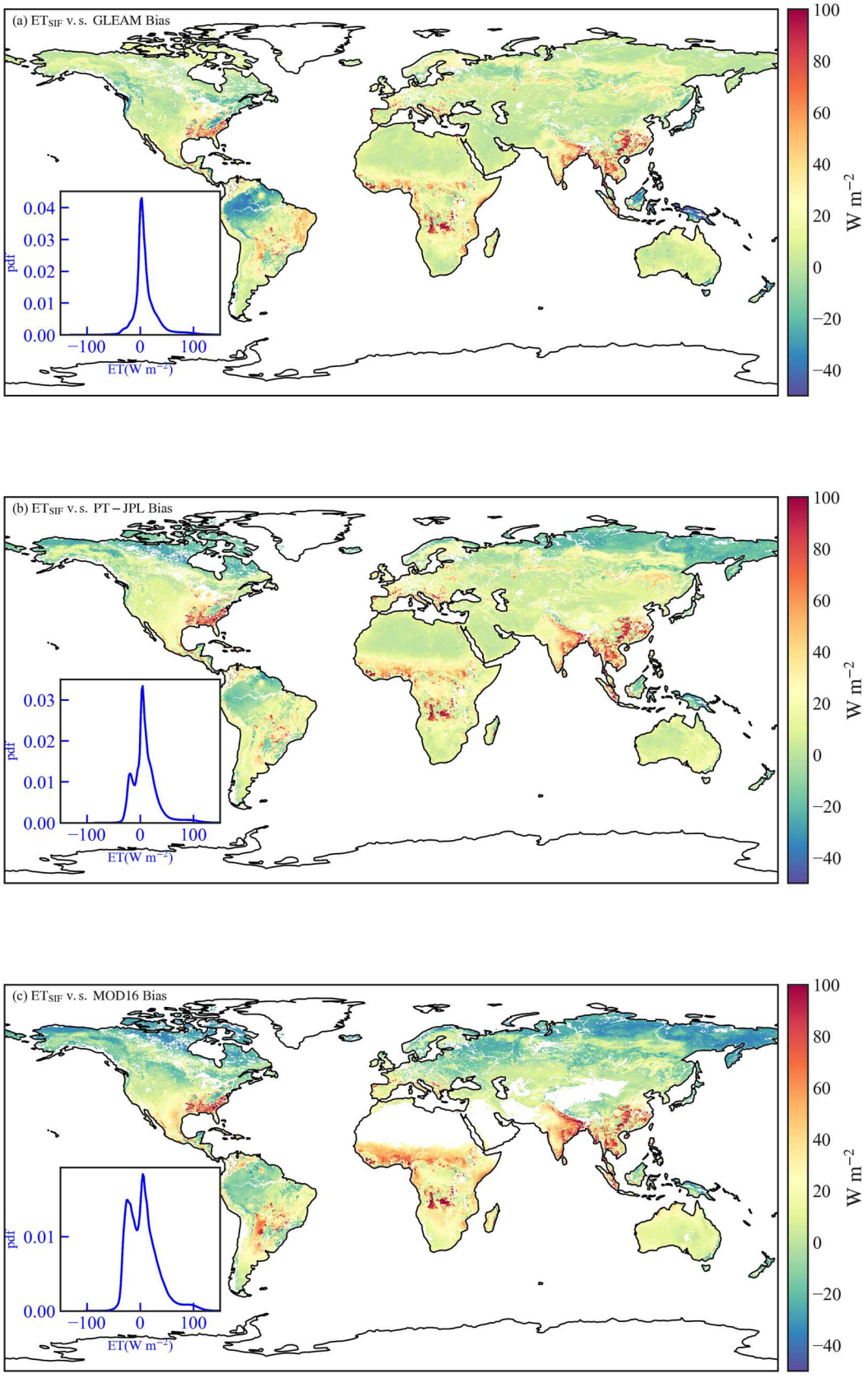

Fig. 9. The spatial distribution of the difference between ET_{SIF} and GLEAM (a), PT-JPL (b) and MOD16 (c) on annual mean time scale; the inset panels show the probability density function (pdf) of these differences.
The comparisons with GLEAM, PT-JPL and MOD16 were conducted for the periods of 2008–2018, 2008–2017 and 2003–2018, respectively. Note that MOD16 does not include sparsely vegetated or non-vegetated areas.

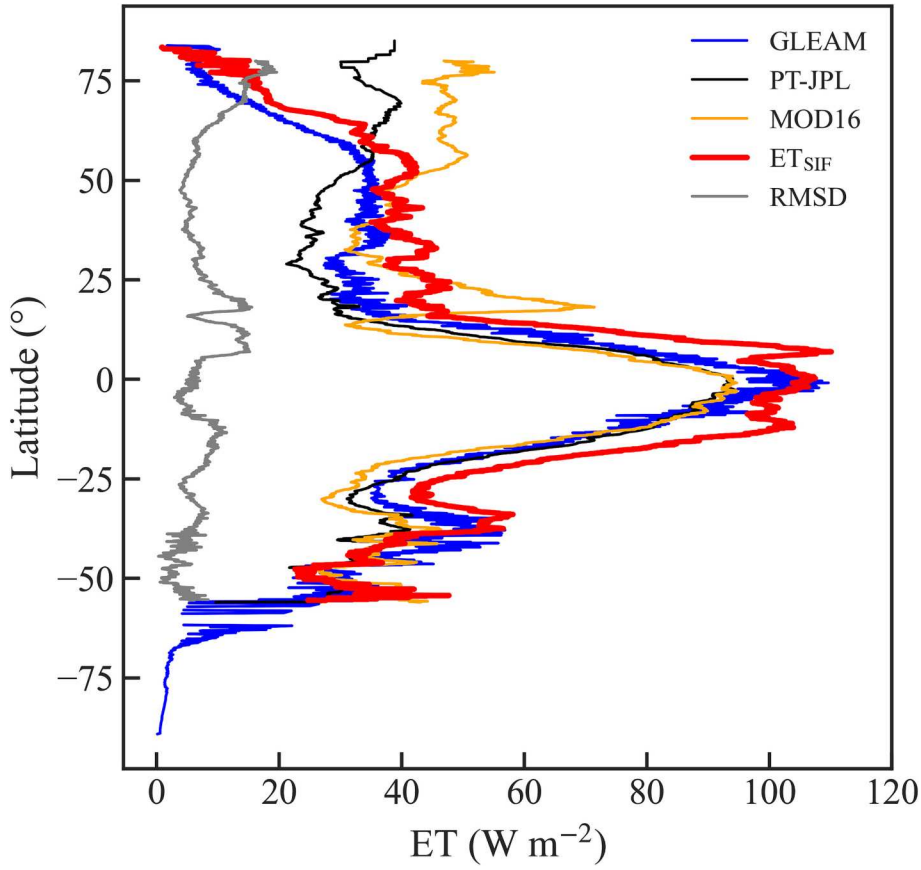

Fig. 10. Comparison of the climatological zonal mean of the global annual ET_{SIF} with the three prior products of GLEAM, PJ-JPL and MOD16.
The grey line represents the Root Mean Square Difference (RMSD) of the four products. Note that all available records of the corresponding ET products are used for this evaluation, but MOD16 ET product does not include sparsely vegetated and non-vegetated areas.

FLUXNET database lacks sites for parameter calibrations for this PFT. Using a mean of the parameter is likely to result in biases in Australia and parts of Asia and southern Africa. The sensitivity of transpiration to the two free parameters together with the input variables are evaluated here using the Sobol' (2001) sensitivity analysis method, which decomposes the model output variance into the sum of variances of the input variables and parameters, and the sensitivity index represents to what extent each parameter (or variable) or the interaction of the

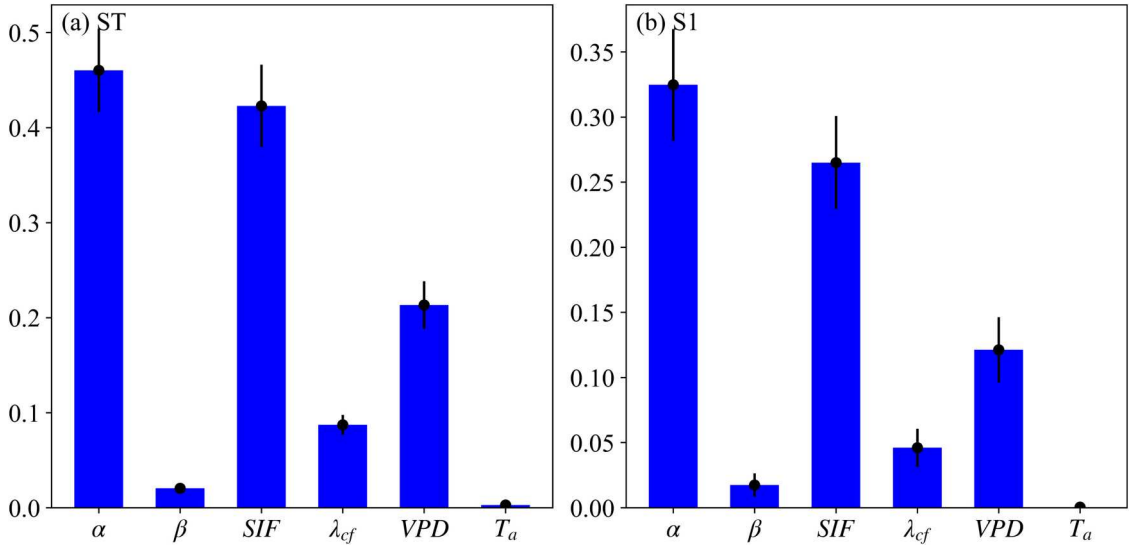

Fig. 11. Sensitivity index of transpiration to the parameters (α, β, and λ_{cf}) and the input variables (SIF, VPD, and Ta).
ST represents the total sensitivity index (a) and S1 represents the first-order sensitivity index (b). In particular, the first-order sensitivity index is evaluated by keeping all other variables (including parameters and input variables) constant, while the total sensitivity index is evaluated by considering variations of all variables (including parameters and input variables); see Sobol' (2001) for the detailed descriptions. Black line represents the 95% confidence interval.

parameters (or variables) will have on the final output. We found transpiration is sensitive to the parameter α (Fig. 11) followed by the input variables of SIF and VPD, implying that any uncertainty associated with the parameter α will easily translate into the uncertainty in transpiration and evapotranspiration estimates. Thus, the accuracy of the parameter α largely determines the overall quality of ET_{SIF}.

Global ET estimation has advanced rapidly over the past decades, especially when combining remote sensing products with energy balance- and meteorologically based models (Bastiaanssen et al., 1998; Su, 2002; Fisher et al., 2008; Mu et al., 2007, 2011). Other data-driven efforts such as upscaling ET measurements at FLUXNET sites to the global scale (Jung et al., 2020) and using machine learning based on FLUXNET and SAPFLUXNET dataset (Koppa et al., 2022) also contributed to global ET assessments. Compared with other high data-demanding methods, ET_{SIF} provides an acceptable estimate using SIF dataset and basic meteorological variables with low data demand and has the potential to advance global ET modelling efforts. Another major advantage is that stomatal conductance is not explicitly required when constraining vegetation transpiration, thereby reducing the associated uncertainty of the model structure. Thus, ET_{SIF} may be viewed as a compromise between the highly parameterized models (e.g., MOD16) and parameter free models (e.g., PT-JPL). The model here based on SIF also provides a possible way for ET partitioning, but independent field measurements of transpiration are required to derive the model parameters to achieve such goal. The acceptable performance of ET_{SIF} at FLUXNET sites lends some confidence to its usage for large-scale ET computations. Needless to say, the accuracy of ET_{SIF} depends on the quality of SIF retrieval, which is impacted by the signal quality, sky condition, among others (e.g., Köhler et al., 2018). Thus, any uncertainty associated with SIF retrieval brings about extra error into ET_{SIF} as SIF is the most sensitive input variable for transpiration in this ET model (see Fig. 11).

5. Summary and conclusion

An evapotranspiration model was developed that combines SIF satellite data and optimality principles for leaf gas exchange. The major novelty of this approach is that the model does not need to parameterize stomatal conductance. The model performance in reproducing eddy-covariance measured ET at FLUXNET sites was acceptable when model parameters related to GPP-SIF were optimized. The derived model parameters at these sites were later employed to determine a global distribution of parameters by relating them to site and climate properties using multiple linear regression. Using ERA5 meteorological input, MODIS LAI and SIF products, the MSWEP precipitation product, the computed evapotranspiration from 2003 through 2018 was in the range of 615–635 mm yr^{-1} with minor but statistically insignificant ET enhancement trend (0.257 mm yr^{-1}) possibly resulting from global greening (Yang et al., 2023). Future developments seek to improve the role of soil moisture stress and hydraulic limitations on the marginal water use efficiency parameter and develop additional constraints on the relation between GPP to SIF. The first global terrestrial ET product mainly driven by SIF may be used to assess antecedent soil moisture conditions, drought monitoring, large-scale runoff and associated changes in the hydrological cycle, among others. The comparisons with other ET products show that large uncertainties generally exist in global ET estimates, thus all global ET products should be treated with caution when dealing with topics on global water cycle.

Author contribution

QZ did the conceptualization of the work, QZ, XL and YZ ran the analysis, QZ did the writing of the original draft, GK assisted in the optimality derivation and implementation, QZ, XL, KZ, YZ, PG, MP and GK reviewed and edited the manuscript.

CRediT authorship contribution statement

Quan Zhang: Writing – review & editing, Writing – original draft, Visualization, Validation, Project administration, Methodology, Investigation, Funding acquisition, Formal analysis, Data curation, Conceptualization. **Xuanqi Liu:** Formal analysis, Data curation. **Kai Zhou:** Formal analysis, Data curation. **Yang Zhou:** Visualization, Data curation. **Pierre Gentine:** Supervision, Methodology, Investigation. **Ming Pan:** Investigation, Data curation. **Gabriel G. Katul:** Supervision, Methodology, Investigation, Conceptualization.

Declaration of competing interest

The authors declare no competing interests.

Data availability

The SIF data is downloaded from https://osf.io/8xqy6/ (see reference Y. Zhang, 2018); the global meteorological forcing is download from ERA5-Land database (https://www.ecmwf.int/en/era5-land); the global land cover is downloaded from https://lpdaac.usgs.gov/products/mcd12c1v061/; the potential evapotranspiration is downloaded from http://josh.yosh.org/datamodels.htm; the global leaf area index (LAI) is downloaded from https://doi.org/10.5067/MODIS/MCD15A3H.006; the MSWEP precipitation dataset is not publicly available yet (contact the co-author M. Pan, m3pan@ucsd.edu or check the reference Beck et al., 2019); the flux data for model parameterization is downloaded from FLUXNET2015 database (https://fluxnet.org/data/fluxnet2015-dataset/); global ET products of GLEAM v3 (https://www.gleam.eu), PT-JPL (http://josh.yosh.org/datamodels.htm) and MOD16 (doi:https://doi.org/10.5067/MODIS/MOD16A2.061) for comparisons are downloaded from their corresponding addresses; our ET_{SIF} product is publicly available at https://figshare.com/s/23964003212879892763 or contacting the corresponding author (Q. Zhang, quan.zhang@whu.edu.cn).

Acknowledgement

We appreciate three anonymous reviewers whose constructive comments lead to great improvement of our work. The study was supported by the National Natural Science Foundation of China (nos. 42371035 and U2243214), and the Provincial Natural Science Foundation of Hubei (no. 2022CFB056). PG acknowledges funding from NASA transpiration partitioning grant 80NSSC18K0998. GK is supported by the US National Science Foundation (NSF-AGS-2028633) and the US Department of Energy (DE-SC0022072).

Appendix A. Supplementary data

Supplementary data to this article can be found online at https://doi.org/10.1016/j.rse.2024.114061.

References

Alemohammad, S.H., Fang, B., Konings, A.G., Aires, F., Green, J.K., Kolassa, J., et al., 2017. Water, energy, and carbon with artificial neural networks (WECANN): a statistically based estimate of global surface turbulent fluxes and gross primary productivity using solar-induced fluorescence. Biogeosciences. 14, 4101–4124. https://doi.org/10.5194/bg-14-4101-2017.

Anderegg, W.R.L., Wolf, A., Arango-Velez, A., Choat, B., Chmura, D.J., Jansen, S., et al., 2018. Woody plants optimise stomatal behaviour relative to hydraulic risk. Ecol. Lett. 21, 968–977. https://doi.org/10.1111/ele.12962.

Bastiaanssen, W.G.M., Menenti, M., Feddes, R.A., Holtslag, A.A.M., 1998. A remote sensing surface energy balance algorithm for land (SEBAL). 1. Formulation. J. Hydrol. 212-213, 198–212. https://doi.org/10.1016/S0022-1694(98)00253-4.

Beck, H.E., Wood, E.F., Pan, M., Fisher, C.K., Miralles, D.G., van Dijk, A.I.J.M., et al., 2019. MSWEP V2 global 3-hourly 0.1° precipitation: methodology and quantitative assessment. Bull. Am. Meteorol. Soc. 100, 473–500. https://doi.org/10.1175/BAMS-D-17-0138.1.

Burchard-Levine, V., Nieto, H., Riaño, D., Kustas, W.P., Migliavacca, M., El-Madany, T.S., et al., 2022. A remote sensing-based three-source energy balance model to improve global estimations of evapotranspiration in semi-arid tree-grass ecosystems. Glob. Chang. Biol. 28, 1493–1515. https://doi.org/10.1111/gcb.16002.

Cui, Y., Jia, L., Hu, G., Zhou, J., 2015. Mapping of interception loss of vegetation in the Heihe river basin of China using remote sensing observations. IEEE Geosci. Remote Sens. Lett. 12, 23–27. https://doi.org/10.1109/LGRS.2014.2324635.

Damm, A., Roethlin, S., Fritsche, L., 2018. Towards advanced retrievals of plant transpiration using sun-induced chlorophyll fluorescence: first considerations. In: IGARSS 2018–2018 IEEE International Geoscience and Remote Sensing Symposium, pp. 5983–5986. https://doi.org/10.1109/IGARSS.2018.8518974.

Damm, A., Haghighi, E., Paul-Limoges, E., van der Tol, C., 2021. On the seasonal relation of sun-induced chlorophyll fluorescence and transpiration in a temperate mixed forest. Agric. For. Meteorol. 304-305, 108386 https://doi.org/10.1016/j.agrformet.2021.108386.

Eagleson, P.S., 1981. Land surface processes in atmospheric General Circulation Models. Cambridge University Press.

Ellsworth, D.S., Oren, R., Huang, C., Phillips, N., Hendrey, G.R., 1995. Leaf and canopy responses to elevated CO_2 in a pine forest under free-air CO_2 enrichment. Oecologia. 104, 139–146. https://doi.org/10.1007/BF00328578.

Farquhar, G.D., Lloyd, J., Taylor, J.A., Flanagan, L.B., Syvertsen, J.P., Hubick, K.T., et al., 1993. Vegetation effects on the isotope composition of oxygen in atmospheric CO_2. Nature. 363, 439–443. https://doi.org/10.1038/363439a0.

Fisher, J.B., Tu, K.P., Baldocchi, D.D., 2008. Global estimates of the land–atmosphere water flux based on monthly AVHRR and ISLSCP-II data, validated at 16 FLUXNET sites. Remote Sens. Environ. 112, 901–919. https://doi.org/10.1016/j.rse.2007.06.025.

Frankenberg, C., O'Dell, C., Berry, J., Guanter, L., Joiner, J., Köhler, P., et al., 2014. Prospects for chlorophyll fluorescence remote sensing from the orbiting carbon observatory-2. Remote Sens. Environ. 147, 1–12. https://doi.org/10.1016/j.rse.2014.02.007.

Gash, J.H.C., 1979. An analytical model of rainfall interception by forests. Q. J. R. Meteorol. Soc. 105, 43–55. https://doi.org/10.1002/qj.49710544304.

Gash, J.H.C., Lloyd, C.R., Lachaud, G., 1995. Estimating sparse forest rainfall interception with an analytical model. J. Hydrol. 170, 79–86. https://doi.org/10.1016/0022-1694(95)02697-N.

Gentine, P., Entekhabi, D., Polcher, J., 2010. Spectral behaviour of a coupled land-surface and boundary-layer system. Bound.-Layer Meteorol. 134, 157–180. https://doi.org/10.1007/s10546-009-9433-z.

Gentine, P., Polcher, J., Entekhabi, D., 2011. Harmonic propagation of variability in surface energy balance within a coupled soil-vegetation-atmosphere system. Water Resour. Res. 47 https://doi.org/10.1029/2010WR009268.

Gu, L., Han, J., Wood, J.D., Chang, C.Y.Y., Sun, Y., 2019. Sun-induced Chl fluorescence and its importance for biophysical modeling of photosynthesis based on light reactions. New Phytol. 223, 1179–1191. https://doi.org/10.1111/nph.15796.

Guan, K., Berry, J.A., Zhang, Y., Joiner, J., Guanter, L., Badgley, G., et al., 2016. Improving the monitoring of crop productivity using spaceborne solar-induced fluorescence. Glob. Chang. Biol. 22, 716–726. https://doi.org/10.1111/gcb.13136.

Guanter Palomar, L., 2006. New Algorithms for Atmospheric Correction and Retrieval of Biophysical Parameters in Earth Observation: Application to ENVISAT/MERIS Data. http://www.tesisenred.net/TDX-0112110-173447.

Guanter, L., Frankenberg, C., Dudhia, A., Lewis, P.E., Gómez-Dans, J., Kuze, A., et al., 2012. Retrieval and global assessment of terrestrial chlorophyll fluorescence from GOSAT space measurements. Remote Sens. Environ. 121, 236–251. https://doi.org/10.1016/j.rse.2012.02.006.

Guanter, L., Zhang, Y., Jung, M., Joiner, J., Voigt, M., Berry, J.A., et al., 2014. Global and time-resolved monitoring of crop photosynthesis with chlorophyll fluorescence. Proc. Natl. Acad. Sci. 111, E1327–E1333. https://doi.org/10.1073/pnas.1320008111.

Hamazaki, T., Kaneko, Y., Kuze, A., Kondo, K., 2005. Fourier transform spectrometer for greenhouse gases observing satellite (GOSAT). Proc.SPIE 5659, 73–80. https://doi.org/10.1117/12.581198.

Hersbach, H., Bell, B., Berrisford, P., Hirahara, S., Horányi, A., Muñoz-Sabater, J., et al., 2020. The ERA5 global reanalysis. Q. J. R. Meteorol. Soc. 146, 1999–2049. https://doi.org/10.1002/qj.3803.

Imasu, R., Matsunaga, T., Nakajima, M., Yoshida, Y., Shiomi, K., Morino, I., et al., 2023. Greenhouse gases observing SATellite 2 (GOSAT-2): mission overview. Prog. Earth Planet. Sci. 10, 33. https://doi.org/10.1186/s40645-023-00562-2.

Jeong, S.-J., Schimel, D., Frankenberg, C., Drewry, D.T., Fisher, J.B., Verma, M., et al., 2017. Application of satellite solar-induced chlorophyll fluorescence to understanding large-scale variations in vegetation phenology and function over northern high latitude forests. Remote Sens. Environ. 190, 178–187. https://doi.org/10.1016/j.rse.2016.11.021.

Joiner, J., Guanter, L., Lindstrot, R., Voigt, M., Vasilkov, A.P., Middleton, E.M., et al., 2013. Global monitoring of terrestrial chlorophyll fluorescence from moderate spectral resolution near-infrared satellite measurements: methodology, simulations, and application to GOME-2. Atmos. Measur. Techniques Discuss. 6, 3883–3930. https://doi.org/10.5194/amt-6-2803-2013.

Jung, M., Reichstein, M., Ciais, P., Seneviratne, S.I., Sheffield, J., Goulden, M.L., et al., 2010. Recent decline in the global land evapotranspiration trend due to limited moisture supply. Nature. 467, 951–954. https://doi.org/10.1038/nature09396.

Jung, M., Schwalm, C., Migliavacca, M., Walther, S., Camps-Valls, G., Koirala, S., et al., 2020. Scaling carbon fluxes from eddy covariance sites to globe: synthesis and evaluation of the FLUXCOM approach. Biogeosciences. 17, 1343–1365. https://doi.org/10.5194/bg-17-1343-2020.

Katul, G.G., Schieldge, J., Hsieh, C.I., Vidakovic, B., 1998. Skin temperature perturbations induced by surface layer turbulence above a grass surface. Water Resour. Res. 34 (5), 1265–1274. https://doi.org/10.1029/98WR00293.

Katul, G.G., Ellsworth, D.S., Lai, C.T., 2000. Modelling assimilation and intercellular CO_2 from measured conductance: a synthesis of approaches. Plant Cell Environ. 23, 1313–1328. https://doi.org/10.1046/j.1365-3040.2000.00641.x.

Katul, G.G., Palmroth, S., Oren, R.A.M., 2009. Leaf stomatal responses to vapour pressure deficit under current and CO_2-enriched atmosphere explained by the economics of gas exchange. Plant Cell Environ. 32, 968–979. https://doi.org/10.1111/j.1365-3040.2009.01977.x.

Katul, G.G., Manzoni, S., Palmroth, S., Oren, R., 2010. A stomatal optimization theory to describe the effects of atmospheric CO_2 on leaf photosynthesis and transpiration. Ann. Bot. 105, 431–442. https://doi.org/10.1093/aob/mcp292.

Köhler, P., Frankenberg, C., Magney, T.S., Guanter, L., Joiner, J., Landgraf, J., 2018. Global retrievals of solar-induced chlorophyll fluorescence with TROPOMI: first results and intersensor comparison to OCO-2. Geophys. Res. Lett. 45, 10–456. https://doi.org/10.1029/2018GL079031.

Koppa, A., Rains, D., Hulsman, P., Poyatos, R., Miralles, D.G., 2022. A deep learning-based hybrid model of global terrestrial evaporation. Nat. Commun. 13, 1912. https://doi.org/10.1038/s41467-022-29543-7.

Lin, C., Gentine, P., Frankenberg, C., Zhou, S., Kennedy, D., Li, X., 2019. Evaluation and mechanism exploration of the diurnal hysteresis of ecosystem fluxes. Agric. For. Meteorol. 278, 107642 https://doi.org/10.1016/j.agrformet.2019.107642.

Liu, Y., Flournoy, O., Zhang, Q., Novick, K.A., Koster, R.D., Konings, A.G., 2022. Canopy height and climate dryness parsimoniously explain spatial variation of unstressed stomatal conductance. Geophys. Res. Lett. 49 https://doi.org/10.1029/2022GL099339 e2022GL099339.

Lloyd, J., Farquhar, G.D., 1994. ^{13}C discrimination during CO_2 assimilation by the terrestrial biosphere. Oecologia. 99, 201–215. https://doi.org/10.1007/BF00627732.

Lu, X., Liu, Z., An, S., Miralles, D.G., Maes, W., Liu, Y., et al., 2018. Potential of solar-induced chlorophyll fluorescence to estimate transpiration in a temperate forest. Agric. For. Meteorol. 252, 75–87. https://doi.org/10.1016/j.agrformet.2018.01.017.

Manzoni, S., Vico, G., Katul, G., Fay, P.A., Polley, W., Palmroth, S., et al., 2011. Optimizing stomatal conductance for maximum carbon gain under water stress: a meta-analysis across plant functional types and climates. Funct. Ecol. 25, 456–467. https://doi.org/10.1111/j.1365-2435.2010.01822.x.

Manzoni, S., Vico, G., Palmroth, S., Porporato, A., Katul, G., 2013. Optimization of stomatal conductance for maximum carbon gain under dynamic soil moisture. Adv. Water Resour. 62, 90–105. https://doi.org/10.1016/j.advwatres.2013.09.020.

Martens, B., Miralles, D.G., Lievens, H., Van Der Schalie, R., De Jeu, R.A.M., Fernández-Prieto, D., et al., 2017. GLEAM v3: satellite-based land evaporation and root-zone soil moisture. Geosci. Model Dev. 10, 1903–1925. https://doi.org/10.5194/gmd-10-1903-2017.

McEvoy, D.J., Huntington, J.L., Mejia, J.F., Hobbins, M.T., 2016. Improved seasonal drought forecasts using reference evapotranspiration anomalies. Geophys. Res. Lett. 43, 377–385. https://doi.org/10.1002/2015GL067009.

Monteith, J.L., 1965. Evaporation and environment. Symp. Soc. Exp. Biol. 19, 205–234.

Mrad, A., Sevanto, S., Domec, J.C., Liu, Y., Nakad, M., Katul, G.G., 2019. A dynamic optimality principle for water use strategies explains isohydric to anisohydric plant responses to drought. Front. Forests Global Change 2, 49. https://doi.org/10.3389/ffgc.2019.00049.

Mu, Q., Heinsch, F.A., Zhao, M., Running, S.W., 2007. Development of a global evapotranspiration algorithm based on MODIS and global meteorology data. Remote Sens. Environ. 111, 519–536. https://doi.org/10.1016/j.rse.2007.04.015.

Mu, Q., Zhao, M., Running, S.W., 2011. Improvements to a MODIS global terrestrial evapotranspiration algorithm. Remote Sens. Environ. 115, 1781–1800. https://doi.org/10.1016/j.rse.2011.02.019.

Norman, J.M., Kustas, W.P., Humes, K.S., 1995. Source approach for estimating soil and vegetation energy fluxes in observations of directional radiometric surface temperature. Agric. For. Meteorol. 77, 263–293. https://doi.org/10.1016/0168-1923(95)02265-Y.

Novick, K.A., Oren, R., Stoy, P.C., Siqueira, M.B.S., Katul, G.G., 2009. Nocturnal evapotranspiration in eddy-covariance records from three co-located ecosystems in the southeastern US: implications for annual fluxes. Agric. For. Meteorol. 149 (9), 1491–1504. https://doi.org/10.1016/j.agrformet.2009.04.005.

Oki, T., Kanae, S., 2006. Global hydrological cycles and world water resources. science. 313, 1068–1072. https://doi.org/10.1126/science.1128845.

Pastorello, G., Trotta, C., Canfora, E., Chu, H., Christianson, D., Cheah, Y.-W., et al., 2020. The FLUXNET2015 dataset and the ONEFlux processing pipeline for eddy covariance data. Sci. Data. 7, 225. https://doi.org/10.1038/s41597-020-0534-3.

Penman, H.L., 1948. Natural evaporation from open water, bare soil and grass. Proceed. Royal Soc. Lond. Ser. A Math. Phys. Sci. 193, 120–145. https://doi.org/10.1098/rspa.1948.0037.

Pierrat, Z.A., Bortnik, J., Johnson, B., Barr, A., Magney, T., Bowling, D.R., et al., 2022. Forests for forests: combining vegetation indices with solar-induced chlorophyll fluorescence in random forest models improves gross primary productivity prediction in the boreal forest. Environ. Res. Lett. 17, 125006 https://doi.org/10.1088/1748-9326/aca5a0.

Priestley, C.H.B., Taylor, R.J., 1972. On the assessment of surface heat flux and evaporation using large-scale parameters. Mon. Weather Rev. 100, 81–92. https://doi.org/10.1175/1520-0493(1972)100<0081:OTAOSH>2.3.CO;2.

Purdy, A.J., Fisher, J.B., Goulden, M.L., Colliander, A., Halverson, G., Tu, K., et al., 2018. SMAP soil moisture improves global evapotranspiration. Remote Sens. Environ. 219, 1–14. https://doi.org/10.1016/j.rse.2018.09.023.

Sellers, P.J., Berry, J.A., Collatz, G.J., Field, C.B., Hall, F.G., 1992. Canopy reflectance, photosynthesis, and transpiration. III. A reanalysis using improved leaf models and a new canopy integration scheme. Remote Sens. Environ. 42, 187–216. https://doi.org/10.1016/0034-4257(92)90102-P.

Sellers, P.J., Randall, D.A., Collatz, G.J., Berry, J.A., Field, C.B., Dazlich, D.A., et al., 1996. A revised land surface parameterization (SiB2) for atmospheric GCMs. Part I: model formulation. J. Clim. 9, 676–705. https://doi.org/10.1175/1520-0442(1996)009<0676:ARLSPF>2.0.CO;2.

Shan, N., Ju, W., Migliavacca, M., Martini, D., Guanter, L., Chen, J., et al., 2019. Modeling canopy conductance and transpiration from solar-induced chlorophyll fluorescence. Agric. For. Meteorol. 268, 189–201. https://doi.org/10.1016/j.agrformet.2019.01.031.

Sobol, I.M., 2001. Global sensitivity indices for non-linear mathematical models and their Monte Carlo estimates. Math. Comput. Simul. 55, 271–280. https://doi.org/10.1016/S0378-4754(00)00270-6.

Su, Z., 2002. The Surface Energy Balance System (SEBS) for estimation of turbulent heat fluxes. Hydrol. Earth Syst. Sci. 6, 85–100. https://doi.org/10.5194/hess-6-85-2002.

Sun, Y., Fu, R., Dickinson, R., Joiner, J., Frankenberg, C., Gu, L., et al., 2015. Drought onset mechanisms revealed by satellite solar-induced chlorophyll fluorescence: insights from two contrasting extreme events. J. Geophys. Res. Biogeosci. 120, 2427–2440. https://doi.org/10.1002/2015JG003150.

Sun, Y., Gu, L., Wen, J., van der Tol, C., Porcar-Castell, A., Joiner, J., et al., 2023. From remotely sensed solar-induced chlorophyll fluorescence to ecosystem structure, function, and service: part I—Harnessing theory. Glob. Chang. Biol. 29, 2926–2952. https://doi.org/10.1111/gcb.16634.

Taylor, T.E., Eldering, A., Merrelli, A., Kiel, M., Somkuti, P., Cheng, C., et al., 2020. OCO-3 early mission operations and initial (vEarly) XCO_2 and SIF retrievals. Remote Sens. Environ. 251, 112032 https://doi.org/10.1016/j.rse.2020.112032.

Volpe, V., Manzoni, S., Marani, M., Katul, G., 2011. Leaf conductance and carbon gain under salt-stressed conditions. J. Geophys. Res. Biogeosci. 116 https://doi.org/10.1029/2011JG001848.

Wan, L., Zhang, Q., Cheng, L., Liu, Y., Qin, S., Xu, J., et al., 2023. What determines the time lags of sap flux with solar radiation and vapor pressure deficit? Agric. For. Meteorol. 333, 109414 https://doi.org/10.1016/j.agrformet.2023.109414.

Wang, Y., Sperry, J.S., Anderegg, W.R.L., Venturas, M.D., Trugman, A.T., 2020. A theoretical and empirical assessment of stomatal optimization modeling. New Phytol. 227, 311–325. https://doi.org/10.1111/nph.16572.

Way, D.A., Katul, G.G., Manzoni, S., Vico, G., 2014. Increasing water use efficiency along the C3 to C4 evolutionary pathway: a stomatal optimization perspective. J. Exp. Bot. 65, 3683–3693. https://doi.org/10.1093/jxb/eru205.

Wei, X., Wang, X., Wei, W., Wan, W., 2018. Use of sun-induced chlorophyll fluorescence obtained by OCO-2 and GOME-2 for GPP estimates of the Heihe River basin, China. Remote Sens. 10, 2039. https://doi.org/10.3390/rs10122039.

Yan, H., Wang, S.Q., Billesbach, D., Oechel, W., Zhang, J.H., Meyers, T., et al., 2012. Global estimation of evapotranspiration using a leaf area index-based surface energy and water balance model. Remote Sens. Environ. 124, 581–595. https://doi.org/10.1016/j.rse.2012.06.004.

Yang, Y., Long, D., Shang, S., 2013. Remote estimation of terrestrial evapotranspiration without using meteorological data. Geophys. Res. Lett. 40, 3026–3030. https://doi.org/10.1002/grl.50450.

Yang, X., Tang, J., Mustard, J.F., Lee, J.-E., Rossini, M., Joiner, J., et al., 2015. Solar-induced chlorophyll fluorescence that correlates with canopy photosynthesis on diurnal and seasonal scales in a temperate deciduous forest. Geophys. Res. Lett. 42, 2977–2987. https://doi.org/10.1002/2015GL063201.

Yang, Y., Roderick, M.L., Guo, H., Miralles, D., Zhang, L., Fatichi, S., et al., 2023. Evapotranspiration on a greening earth. Nat. Rev. Earth Environ. 4, 626–641. https://doi.org/10.1038/s43017-023-00464-3.

Yoshida, Y., Joiner, J., Tucker, C., Berry, J., Lee, J.E., Walker, G., et al., 2015. The 2010 Russian drought impact on satellite measurements of solar-induced chlorophyll fluorescence: insights from modeling and comparisons with parameters derived from satellite reflectances. Remote Sens. Environ. 166, 163–177. https://doi.org/10.1016/j.rse.2015.06.008.

Yuan, W., Liu, S., Yu, G., Bonnefond, J.-M., Chen, J., Davis, K., et al., 2010. Global estimates of evapotranspiration and gross primary production based on MODIS and global meteorology data. Remote Sens. Environ. 114, 1416–1431. https://doi.org/10.1016/j.rse.2010.01.022.

Zarco-Tejada, P.J., Berni, J.A.J., Suárez, L., Sepulcre-Cantó, G., Morales, F., Miller, J.R., 2009. Imaging chlorophyll fluorescence with an airborne narrow-band multispectral camera for vegetation stress detection. Remote Sens. Environ. 113, 1262–1275. https://doi.org/10.1016/j.rse.2009.02.016.

Zhang, Y., Guanter, L., Berry, J.A., Joiner, J., van der Tol, C., Huete, A., et al., 2014a. Estimation of vegetation photosynthetic capacity from space-based measurements of chlorophyll fluorescence for terrestrial biosphere models. Glob. Chang. Biol. 20, 3727–3742. https://doi.org/10.1111/gcb.12664.

Zhang, L., Hu, Z., Fan, J., Zhou, D., Tang, F., 2014b. A meta-analysis of the canopy light extinction coefficient in terrestrial ecosystems. Front. Earth Sci. 8, 599–609. https://doi.org/10.1007/s11707-014-0446-7.

Zhang, Q., Manzoni, S., Katul, G., Porporato, A., Yang, D., 2014c. The hysteretic evapotranspiration—vapor pressure deficit relation. J. Geophys. Res. Biogeosci. 119, 125–140. https://doi.org/10.1002/2013JG002484.

Zhang, Y., Guanter, L., Berry, J.A., van der Tol, C., Yang, X., Tang, J., et al., 2016a. Model-based analysis of the relationship between sun-induced chlorophyll fluorescence and gross primary production for remote sensing applications. Remote Sens. Environ. 187, 145–155. https://doi.org/10.1016/j.rse.2016.10.016.

Zhang, K., Kimball, J.S., Running, S.W., 2016b. A review of remote sensing based actual evapotranspiration estimation. WIREs Water. 3, 834–853. https://doi.org/10.1002/wat2.1168.

Zhang, Y., Joiner, J., Alemohammad, S.H., Zhou, S., Gentine, P., 2018. A global spatially contiguous solar-induced fluorescence (CSIF) dataset using neural networks. Biogeosciences. 15, 5779–5800. https://doi.org/10.5194/bg-15-5779-2018.

Zhang, Q., Ficklin, D.L., Manzoni, S., Wang, L., Way, D., Phillips, R.P., et al., 2019. Response of ecosystem intrinsic water use efficiency and gross primary productivity to rising vapor pressure deficit. Environ. Res. Lett. 14, 074023 https://doi.org/10.1088/1748-9326/ab2603.

Zhang, Q., Barnes, M., Benson, M., Burakowski, E., Oishi, A.C., Ouimette, A., et al., 2020. Reforestation and surface cooling in temperate zones: mechanisms and implications. Glob. Chang. Biol. 26, 3384–3401. https://doi.org/10.1111/gcb.15069.

Zheng, C., Jia, L., 2019. Global canopy rainfall interception loss derived from satellite earth observations. Ecohydrology. 13, e2186 https://doi.org/10.1002/eco.2186.

Zhou, K., Zhang, Q., Xiong, L., Gentine, P., 2022. Estimating evapotranspiration using remotely sensed solar-induced fluorescence measurements. Agric. For. Meteorol. 314, 108800 https://doi.org/10.1016/j.agrformet.2021.108800.